AD-A215 540

MICROSTRUCTURAL COMPATIBILITY OF AN Al-Li-Cu-Mg-Zr ALLOY EXPOSED TO CORROSIVE ENVIRONMENTS

T. S. Srivatsan

Materials Modification Inc.

Falls Church Virginia 22044

FINAL REPORT
(Period: 15 November 1986 to 15 May 1987)
Contract No. N60921-86-M-7570
Department of the Navy
Naval Surface Weapons Center
Silver Spring, Maryland 20903

June 01, 1987

Naval Surface Weapons Center
Dahlgren, Va. • White Oak, Md.

AD-A215 540

REPORT DOCUMENTATION PAGE

1a REPORT SECURITY CLASSIFICATION	1b RESTRICTIVE MARKINGS
2a SECURITY CLASSIFICATION AUTHORITY	3 DISTRIBUTION / AVAILABILITY OF REPORT Approved for public release. Distribution unlimited.
2b DECLASSIFICATION / DOWNGRADING SCHEDULE Unclassified	
4 PERFORMING ORGANIZATION REPORT NUMBER(S) MMI-SRI-0002-87	5 MONITORING ORGANIZATION REPORT NUMBER(S)
6a NAME OF PERFORMING ORGANIZATION Materials Modification Inc. / 6b OFFICE SYMBOL (If applicable)	7a NAME OF MONITORING ORGANIZATION Naval Surface Weapons Center.
6c ADDRESS (City, State, and ZIP Code) 2946, Sleepy Hollow Road; Suite # 2H Falls Church, VA 22044	7b ADDRESS (City, State, and ZIP Code) Metallurgist, Metallic Materials Div. (R-32) White Oak Laboratories, Silver Spring MD 20903-5000; Attn. Mr. Dave Divecha
8a NAME OF FUNDING / SPONSORING ORGANIZATION Naval Surface Weapons Center / 8b OFFICE SYMBOL (If applicable)	9 PROCUREMENT INSTRUMENT IDENTIFICATION NUMBER N60921-86-M-7570
8c ADDRESS (City, State, and ZIP Code) White Oak Laboratories, Silver Spring MD 20903-5000	10 SOURCE OF FUNDING NUMBERS PROGRAM ELEMENT NO / PROJECT NO / TASK NO / WORK UNIT ACCESSION NO

11 TITLE (Include Security Classification)
MICROSTRUCTURAL COMPATIBILITY OF AN Al-Li-Cu-Mg-Zr ALLOY EXPOSED TO CORROSIVE ENVIRONMENTS.

12 PERSONAL AUTHOR(S)
Dr. Srivatsan, T.S.

13a TYPE OF REPORT	13b TIME COVERED	14 DATE OF REPORT (Year, Month, Day)	15 PAGE COUNT
Final	FROM 15Nov 86 TO 15May87	June 01, 1987	-84-

16 SUPPLEMENTARY NOTATION

17 COSATI CODES			18 SUBJECT TERMS (Continue on reverse if necessary and identify by block number)
FIELD	GROUP	SUB-GROUP	Aluminum Alloy, fracture, microstructure, environment, corrosion

19 ABSTRACT (Continue on reverse if necessary and identify by block number)

This investigation was undertaken to evaluate the influence of microstructure on the fracture characteristics and the general corrosion resistance of a quarternary Al-2.8Li-1.3Cu-0.7Mg alloy 8090 in the peak-aged condition in environments spanning an entire range of aggressiveness.

In the aging condition studied, fracture was predominantly low energy intergranular and intersubgranular separation. The fracture process was observed to be governed by a complex interplay of several concurrent and mutually competitive factors involving intrinsic microstructural features, the matrix deformation characteristics and grain boundary failure.

The corrosion rate was established through weight loss measurements using ASTM G31 coupons. Immersion test results indicate that weight loss occurred in both acidic and basic solutions. Corrosion rates expressed in mils per year (mpy) were observed to decrease with time of immersion in solution. The pH of the solutions changed during the

20 DISTRIBUTION / AVAILABILITY OF ABSTRACT ☐ UNCLASSIFIED/UNLIMITED ☐ SAME AS RPT ☐ DTIC USERS	21 ABSTRACT SECURITY CLASSIFICATION
22a NAME OF RESPONSIBLE INDIVIDUAL A. Einbinder	22b TELEPHONE (Include Area Code) (202) 394-1870 / 22c OFFICE SYMBOL R28

DD FORM 1473, 84 MAR — 83 APR edition may be used until exhausted. All other editions are obsolete.

SECURITY CLASSIFICATION OF THIS PAGE

period of testing. Weight loss measurements, optical electron microscopy and scanning electron microscopy observations indicate that the coupons of the quarternary alloy begin to corrode rapidly during the initial hours of immersion in the solution followed by a period of uniform corrosion in which pitting dominates. In highly hostile environments (aqueous solutions) the alloy appears to undergo enhanced corrosion along grain boundaries. This is also evident after prolonged immersion in less hostile environments. Pitting was observed to occur at the second-phase particles dispersed in the matrix, and at the grain boundary precipitate particles. The results of the immersion test suggest the operation of several concurrent and competing processes involving intrinsic microstructural features, alloy chemistry and corrosion science.

MICROSTRUCTURAL COMPATIBILITY OF AN Al-Li-Cu-Mg-Zr ALLOY EXPOSED TO CORROSIVE ENVIRONMENTS

T. S. Srivatsan

Materials Modification Inc.
Falls Church Virginia 22044

FINAL REPORT
(Period: 15 November 1986 to 15 May 1987)
Contract No. N60921-86-M-7570
Department of the Navy
Naval Surface Weapons Center
Silver Spring, Maryland 20903

June 01, 1987

Naval Surface Weapons Center
Dahlgren, Va. • White Oak, Md.

TABLE OF CONTENTS

TABLE OF CONTENTS (Cont.)

FOREWORD

This final technical report covers activities performed during the period 15 November 1986 to 15 May 1987, for the Naval Surface Weapons Center under U. S. Navy Contract N60921-86-M-7570.

The contract is with Materials Modification Inc.,(MMI), Falls Church, Virginia. Dr. A. P. Divecha is the U. S. Navy contract monitor. This report has been prepared by Dr. T. S. Srivatsan, MMI Principal Investigator and Project Manager for the program.

ACKNOWLEDGEMENTS

The author would like to acknowledge with thanks Dr. T. S. Sudarshan and Colonel (R) Donald Tapscott for their guidance, suggestions and support.

I would also like to extend my thanks and appreciation to Mr. A. Frefer, Professor T. Alan Place and Professor G. E. Bobeck of the University of Idaho for the help extended during the course of this work.

It is a pleasure to thank Mr. S. Bettadapur of the Naval Air Systems Command for his sustained interest in this research project and encouragement.

LIST OF TABLES

LIST OF FIGURES

ABSTRACT

This investigation was undertaken to evaluate the influence of microstructure on the fracture characteristics and the general corrosion resistance of a quarternary Al-2.8Li-1.3Cu-0.7Mg alloy 8090 in the peak-aged condition in environments spanning an entire range of aggressiveness.

In the aging condition studied, fracture was predominantly low energy intergranular and intersubgranular separation. The fracture process was observed to be governed by a complex interplay of several concurrent and mutually competitive factors involving intrinsic microstructural features, the matrix deformation characteristics and grain boundary failure.

The corrosion rate was established through weight loss measurements using ASTM G-31 coupons. Immersion test results indicate that weight loss occurred in both acidic and basic solutions. Corrosion rates expressed in mils per year (mpy) were observed to decrease with time of immersion in solution. The pH of the solutions changed during the period of testing. Weight loss measurements, optical microscopy and scanning electron microscopy indicate that the coupons of the quarternary alloy begin to corrode rapidly during the initial hours of immersion in the solution followed by a period of uniform corrosion in which pitting dominates. In highly hostile environments

(solutions) the alloy appears to undergo enhanced corrosion along grain boundaries. This is also evident after prolonged immersion in less hostile environments. Pitting was observed to occur at the second-phase particles dispersed in the matrix, and at the grain boundary precipitates. The results of the immersion test suggest the operation of several concurrent and competing processes involving intrinsic microstructural features, alloy chemistry and corrosion science.

1. INTRODUCTION

Advanced aircraft performance requirements include higher speeds, longer ranges, greater payload capacities, better fuel economy and improved landing capabilities. The critical need to improve the efficiency and performance of aircraft, coupled with continuing emphasis on minimum weight, has prompted interest in the use of lighter and stiffer materials. Lithium-containing aluminum alloys are attractive alternatives to existing high strength aluminum alloys and carbon-fiber composites (CFC) for stiffness-critical airframe structures. The family of aluminum-lithium alloys offers the promise of weight savings in aircraft structural applications and desirable combinations of high strength, decreased densities, increased stiffness, improved thermal stability and good resistance to the propagation of fatigue cracks, have engendered an unprecedented widespread interest in the aerospace industry on account of their potential to replace conventional aluminum alloys. These alloys have been the subject of increased research activity aimed at understanding their various metallurgical, mechanical and corrosion characteristics [1-4].

Magnesium and lithium are the only two elemental additions which when added to aluminum have the effect of decreasing its density. Beryllium also decreases the density of aluminum but it is a health hazard. Lithium is one of the few elements with substantial solubility in aluminum (4.2 wt% at 600^{o}C in a binary aluminum-lithium alloy). The potential for aluminum alloy density reduction through lithium additions is evident by comparing its atomic weight (6.94) with that of aluminum (26.98). Lithium addition to aluminum also causes a significant increase in elastic modulus. For every 1 wt% lithium added to an aluminum alloy up to 4 wt% Li, the density decreases by 3% and the elastic modulus increases by 6% [5]. The specific modulus (modulus of elasticity/weight) of an alloy with 2.8% Li by weight is 21% higher than that of alloy 2024-T351 and 26% higher than that of 7075-T651. The higher specific modulus reduces the rate of fatigue crack growth. The decrease in density is far more effective in reducing structural weight than improved strength, modulus, toughness or fatigue resistance [6].

The potential benefit of lithium additions to aluminum in terms of reduced density, and improved stiffness, combined with high strength (0.2% yield strength > 500 MPa) was first recognized by LeBaron [7] and resulted in the development of the Al-4.5Cu-1.2Li-0.5Mn-0.2Cd alloy, designated 2020 by the Aluminum Association. Besides possessing high strength, low density and an increased elastic modulus, AA 2020 offered freedom from exfoliation corrosion and stress corrosion cracking, thus making it potentially superior to other commercially available aluminum alloys for use in high-performance military aircraft. However, the associated low ductility and inadequate fracture toughness for many potential applications, made the efficient use of alloy 2020 at high stresses inadvisable. This limitation coupled with manufacturing difficulties resulted in its early withdrawal as a commercial alloy.

Various modifications in alloy chemistry and processing techniques have been successfully used in an attempt to improve the ductility of Al-Li-X alloys, while maintaining the benefit of high strength. Ternary solute additions to the aluminum-lithium system such as magnesium, copper and zirconium have been found to have beneficial effects [8]. Magnesium and copper improve the strength of Al-Li alloys by co-precipitating with $\delta'(Al_3Li)$ and/or incorporating lithium to form coherent and partially coherent ternary and more complex matrix strengthening precipitates. Besides, magnesium reduces the solubility of lithium during the early stages of aging and increases the volume fraction of the coherent strengthening precipitate, $\delta' Al_3Li$ [9]. Magnesium also minimizes or eliminates the formation of precipitate free zones (PFZ's) near grain boundaries by precipitating as S" or S' (Al_2CuMg). Zirconium additions to Al-Li-Cu alloys result in the formation of metastable cubic precipitates (Al_3Zr) which are spherical in morphology, coherent with the aluminum matrix and can effectively pin the grain and subgrain boundaries. The cubic Al_3Zr precipitates (referred to from now on as β' and/or dispersoids), aid in retarding subgrain boundary migration and coalescence, and this stabilizes the subgrain structure and inhibits recrystallization. The β' (Al_3Zr) nucleates heterogeneously on dislocations and boundaries [9]. Zirconium additions to lithium-containing aluminum alloys are attractive since they prevent recrystallization without the deleterious effect on corrosion resistance that accompanies manganese additions.

Service experience with lithium-containing aluminum alloys has been limited to AA 2020. This alloy was used for wing skins and horizontal stabilizer on the Mach 2, RA-5C Vigilante fighter aircraft flown by the United States Navy. Alloy 2020 exhibited good corrosion and stress corrosion resistance. A study by Rinker and co-workers [10] on the influence of precipitation heat treatment on the stress corrosion cracking (SCC) resistance of alloy 2020 revealed that the alloy had excellent corrosion resistance in the high strength, peak-aged (PA) temper. Poor SCC resistance was observed for the severely under-aged (UA) temper. The variation in stress corrosion resistance of the alloy with precipitation heat treatment was attributed to a reduction in the electrochemical potential difference between the grain boundary T_1 (Al_2CuLi) precipitates and the matrix during aging [10]. Vasudevan and co-workers at ALCOA [11] evaluated the stress corrosion cracking of ternary Al-Cu-Li-Zr alloys in 3.5% NaCl solution. In particular, the effect of aging and Li:Cu (atomic ratio) was explored in the maximum strength, peak-aged (PA) condition (T651). Results of this study revealed that Al-Cu-Li-Zr alloys showed improved resistance to SCC when compared to the conventional aluminum alloys. The grain boundary precipitates were observed to play an important role in the SCC of Al-Li-Cu alloys. The alloys exhibited improved resistance to SCC growth with an increase in the amount of grain boundary precipitates such as the δ (AlLi) phase, which occurs in alloys having high lithium-content. Christodoulou and co-workers [12] found the degree of SCC susceptibility of binary Al-Li alloys to be dependent on the aging condition, with the peak-aged temper being the most susceptible. These researchers suggested that hydrogen embrittlement may play an important role in the SCC mechanism of binary lithium-containing aluminum alloys [12]. Pizzo and co-workers [13] studied the stress-corrosion behavior of P/M Al-Li alloys containing copper and magnesium. They observed that the stringer oxide particles play an important role in determining SCC behavior of P/M Al-Li-Cu alloys. Other studies have focussed on the corrosion resistance of binary and ternary alloys [14-18]. Stokes and co-workers [19] evaluated the corrosion characteristics of a quarternary Al-Li-Cu-Mg-Zr alloy in marine environments. These researchers observed that the alloy in the peak-aged, maximum strength temper suffered from pitting, crevice corrosion, blistering and exfoliation corrosion [19].

Little is yet known about the corrosion behavior of these alloys in aggressive environments such as sea water. On account of the extremely reactive nature of lithium, alloying aluminum with lithium could result in an alloy which in a moist or saline environment is subject to extensive corrosive attack. The purpose of the present work is to characterize the microstructure, tensile properties, fracture characteristics and the general corrosion characteristics of a quarternary Al-Li-Cu-Mg-Zr alloy, designated as 8090 by the Aluminum Association. The tensile properties were determined in both the longitudinal and transverse directions of the extruded plate. The general corrosion characteristics of the alloy were studied in aqueous environments covering an entire range of aggressiveness (spanning the very acidic to the basic) and correlated with microstructure. The results of such a study provides an understanding of the influence of alloy composition (chemistry) and intrinsic microstructural features such as grain boundaries, constituent particles and grain boundary precipitates on the corrosion behavior of the quarternary alloy.

2. PRECIPITATION CHARACTERISTICS OF Al-Li-Cu-Mg ALLOYS

Aluminum alloys containing lithium as a major alloying element rely upon heat-treatment to develop high strength [20]. Noble and Thompson [21] summarized the precipitation sequence as a two-stage process:

$$\text{Supersaturated solid solution} \longrightarrow \delta' \, (Al_3Li) \longrightarrow \delta \, (AlLi)$$

Maximum strength was found to be associated with the metastable, ordered ($L1_2$ crystal structure) δ' phase which is coherent with the aluminum matrix. Strength of these alloys can be enhanced by the additions of magnesium or copper or both. Peel and co-workers [22] added both these alloying elements to a binary aluminum-lithium alloy resulting in the development of a quarternary Al-Li-Cu-Mg alloy.

The quarternary alloy system is complicated and the phase diagram is as yet unknown. However, recent studies [23-27] have shown that the precipitate structure is similar to those that occur in the ternary Al-Cu-Mg, Al-Li-Mg and Al-Cu-Li systems. During aging of the quarternary alloy, co-precipitation of $\delta'(Al_3Li)$, T_1 (Al_2CuLi) and S' (Al_2CuMg) phases occurs. The precipitation sequence in magnesium-containing Al-Li [28] and Al-Cu [29] alloy systems being:

Supersaturated solid solution $\rightarrow \delta'(Al_3Li) \rightarrow Al_2MgLi$

Supersaturated solid solution $\rightarrow$ S" $\rightarrow$ S'(Al_2CuMg) $\rightarrow$ S (Al_2CuMg)

Of the various phases present in the Al-Li-Cu-Mg alloys, the T_1 and S' precipitates provide major strengthening in addition to strengthening contributions from the homogeneous precipitation of $\delta'(Al_3Li)$. The orientation relationship of the T_1 (Al-Cu-Li system) and S' phases and the matrix in the quarternary alloy is the same as occurs in the ternary alloys.

$$(0001)_{T_1} \parallel (111)_{Al} \; ; \; (1010)_{T_1} \parallel (110)_{Al} \; ; \; (1120)_{T_1} \parallel (211)_{Al}$$
$$[110]_{S'} \parallel [100]_{Al} \; ; \; [010]_{S'} \parallel [021]_{Al} \; ; \; [001]_{S'} \parallel [021]_{Al}$$

The nucleation of the Al_2CuLi (T_1), Al_2Cu (θ') and Al_2CuMg (S') precipitates occurs at dislocations, and deformation prior to aging increases the dislocation density and, thus, the number of nucleating sites for precipitation of phases with large coherency strains [30]. The T_1 and θ' phases have large coherency strains and nucleate preferentially on dislocations when aged below their metastable solvus temperatures, since the strains associated with the dislocations reduce the overall strain energy [31]. A small amount of stretching prior to aging also promotes a homogeneous distribution of smaller matrix strengthening precipitates [8]. Consequently, no significant precipitate free zone due to the T_1 and S' precipitates is likely to result. With prolonged aging, the equilibrium Al_2MgLi, T_2 (Al_6CuLi_3) and S(Al_2CuMg) phases tend to nucleate heterogeneously at planar interfaces, that is, the high angle grain and low angle (subgrain) boundaries, with S (Al_2CuMg) being significantly more dominant than either T_2 and Al_2MgLi [32].

Table 1 summarizes the composition, crystal structure and orientation relationships of some of the precipitate phases likely to be present in the quarternary alloy.

3. MATERIAL AND EXPERIMENTAL PROCEDURES

3.1 Material

The Al-Li-Cu-Mg alloy used in this study was obtained from the Naval Surface Weapons Center, White Oak, Maryland, as extruded plate of cross-section 100 mm x 25 mm in the T851 condition. The chemical composition (in weight percent) of the alloy is given in Table 2.

The iron and silicon elements in the alloy are impurities. During ingot solidification and subsequent processing, these impurities precipitate as insoluble constituent phases Al_3Fe and Al_7Cu_2Fe. The principal strengthening precipitates in ternary Al-Cu-Li alloys are δ' (Al_3Li), T_1 (Al_2CuLi) and θ' (Al_2Cu) [33,34]. In the peak-aged, maximum strength condition the Al-Li-Cu alloys contain precipitate free zones (PFZ's) along grain and subgrain boundaries [35, 36]. Magnesium additions to a ternary Al-Li-Cu alloy provides solid solution strengthening and additional strengthening through the precipitation of S' (Al_2CuMg). It also eliminates the formation of precipitate free zones by precipitating (as S" and S') near grain boundaries.

The heat treatment on the extruded plate consisted of solution treatment at 307°C (586°F) for 30 minutes in a molten salt bath. The alloy was then quenched in water at room temperature, and stretched 2% immediately after solution treatment to: (i) relieve the residual stresses resulting from quenching, and (ii) to promote a heterogeneous nucleation of precipitates during subsequent artificial aging. The alloy was artificially aged in an oil bath at 170°C (338°F) for 32 hours followed by 163°C (325°F) for 40 hours to obtain the maximum strength condition.

3.2 Microstructural Characterization

In order to characterize the size and morphology of the grains, samples for optical microscopy were wet ground on 400 and 600 grit SiC paper and then mechanically polished with 1 micron and 0.05 micron alumina. Grain morphology was revealed using Keller's etch and observed by optical microscopy.

To determine the size and distribution of the soluble precipitates, a hot (50°C) 10% orthophosphoric acid solution was used as the etchant. The specimens were etched for 180 seconds, observed in an optical microscope and photographed using standard bright field technique. A hot bromine etch procedure was used to analyze the size, morphology and distribution of the insoluble and high temperature precipitating phases. The bromine-etch procedure involved submersing samples in a boiling solution mixture of 10% bromine in methanol for 60 seconds. This solution selectively attacks the aluminum matrix and exposes the coarse constituent phases. The etched specimens were examined by scanning electron microscopy (SEM).

3.3 Density

The procedure for experimental measurement of density was based on Archimedes Principle [37]. The weight of a smooth, polished sample was determined in air and immersed (suspended) in distilled water. The difference in weight of the sample in the two mediums is equal to the weight of fluid (distilled water) displaced. The density of distilled water was determined by measuring the weight of a known volume. The density was used to estimate the volume of distilled water displaced by the sample. The density of the sample was evaluated by dividing its weight in air by the volume of fluid (distilled water) it displaced. All weight measurements were performerd using a Mettler Instrument Corporation, Type P163, electronic analytical balance, with a precision of 1×10^{-3} grams.

The predicted density was obtained using the formulation [22]

$$\text{Density (g/cc)} = 2.71 + 0.024\,\text{Cu} + 0.018\,\text{Zn} + 0.022\,\text{Mn} - 0.079\,\text{Li} - 0.01\,\text{Mg} - 0.004\,\text{Si} \quad (1)$$

where the atomic symbol represents the concentration in weight percent. This relationship assumes that the density of the lithium-containing aluminum alloy is the sum of the densities of the constituent elements, weighted by the atomic fraction of the respective elements. It is assumed that each element is in substitutional solid solution in aluminum.

3.4. Tensile Tests

Specimens of circular cross-section were machined from the extruded plate with the loading axis parallel and perpendicular to the extrusion (longitudinal) direction. The specimens were smooth and cylindrical in the gage section, which measured 35 mm in length and 6.35 mm in diameter. Tensile tests were performed on a closed-loop servohydraulic testing machine with an initial strain rate of 6×10^{-4} per second. The tests were conducted under stroke control. The load-displacement curve was recorded on a strip-chart recorder. The diameters of the tensile samples before and after the test were measured using a micrometer.

3.5 Fractography

Fracture surfaces of the tensile specimens were examined in a scanning electron microscope (SEM) so as to determine the predominant fracture mode and to characterize the fine-scale fracture features on the surface.

3.6 Corrosion Testing

In order to investigate the general corrosion characteristics of the alloy, coupon corrosion testing was performed in accordance with ASTM G31. In order to ensure a large surface-to-volume ratio and a small ratio of edge area to total area, coupons were cut from the as-received material to dimensions of 35 mm by 25 mm by 3 mm (Figure 1). Specimens were wet ground using 600 grit SiC paper, mechanically polished with one micron alumina, rinsed in methanol and air dried. The dried specimens were weighed in a Mettler balance to an accuracy of 0.001 grams. Dimension of the specimens were measured using a vernier caliper. The polished specimens were stored in a desiccator until testing.

Distilled water and reagent-grade NaCl were mixed to produce a 3.5% NaCl (0.6 N) solution, referred to henceforth as the stock solution.. The starting pH of the solution was 6.99. Solutions of pH 1 and pH 3 were obtained by adding the required amount of reagent-grade hydrochloric acid to the stock solution. In accordance with ASTM G31, the solutions were not deaerated. Testing was done at ambient-room temperature ($80^{o}F$), laboratory air (Relative Humidity, 65%). In order to ensure an adequate solution volume-to-specimen area, the volume of test solution used was 1000 ml. To minimize contamination of the solution and loss due to evaporation, the beakers were covered with Parafilm during the entire testing period.

The corrosion coupons were mounted on a glass-stand (Figure 2). Each glass-stand having provision for accommodating six coupons. The glass-stand with coupons was immersed in a beaker containing solution of desired pH (Figure 3). On completion of the test for selected time intervals, the coupons were removed, photographed, chemically cleaned, degreased and weighed. The cleaning procedure was in accordance with ASTM G1. The coupons were:

(i) mechanically brushed in order to remove the bulky corrosion products on the surface, and then

(ii) chemically cleaned by immersion in reagent-grade nitric acid for 15 minutes.

The specimens were rinsed in acetone, air-dried and re-weighed in the Mettler balance to an accuracy corresponding to that of the original weighing. Weight differences were then determined. The weight loss or weight gain during the test period is the principal measure of corrosion.

The pH of the solutions were monitored at selected time intervals (every 24 hours). Solution pH measurements were made using a pH meter. From the weight differences, the uniform corrosion rates in mils per year (mpy) were calculated using the relationship:

$$\text{Corrosion rate (mpy)} = [(K \times W)/(A \times T \times D)]. \qquad (2)$$

where:

K = a constant (3.45×10^6)

T = time of exposure in hours

A = the surface area of the coupon in cm^2

W = weight loss or weight gain in grams, to the nearest 1 mg.

D = the density of AA 8090 (g/cc).

Corrosion rates were also determined in milligrams per square decimeter per day (mdd), in which case the constant in the above equation is $2.40 \times 10^6 \times D$.

Coupon testing results are presented as variation of:

(a) solution pH with time (hours),

(b) Weight loss (grams) with Time (hours), and

(c) Corrosion Rate (mpy) with Time (hours).

4. RESULTS and DISCUSSION

4.1 Density

The measured value of density obtained by using the Archimedes Principle was 2.503 grams/cc. The predicted density obtained by using Equation (1) is 2.513 grams/cc. The measured and predicted densities are compared in Figure 5 with a limited selection of aluminum alloys. The density of AA 8090 is compared with the densities of other aluminum alloys in Table 3.

4.2 Microstructure

Examination of the grain structure of the as-received material revealed a partially recrystallized structure (Figure 6) with the unrecrystallized grains flattened and elongated in the longitudinal direction, as a consequence of deformation introduced during extrusion. The transverse grains appeared to have a large aspect ratio (Figure 6). The grain and subgrain boundaries were observed to be decorated with a fine dispersion of second-phase particles that are: (i) the coarse (iron-rich and magnesium-rich) constituent phases, and/or (ii) the equilibrium phases [δ (AlLi), S (Al_2CuMg) and T-type ($Al_xCu_yLi_z$)] (Figures 7 and 8). In an earlier study on an Al-3Cu-1.58Li-0.79Mg-0.2Zr alloy [25], these particles were identified as:

(i) the lithium-rich equilibrium phase T_2 (Al_6CuLi_3) that occurs in the form of massive round particles, and

(ii) the S (Al_2CuMg) phase.

At higher magnification, the nonsoluble and partially soluble constituent particles were observed to be stratified and distributed in the extrusion direction of the plate (Figure 8). Figure 9 is an optical micrograph which reveals a non-uniform size and distribution of the subgrains in the longitudinal (extrusion) direction. At regular intervals 'clumping' of the constituent particles was observed in the L direction of the plate (Figure 10). The distribution of larger insoluble constituent particles is revealed by bromine etching (Figure 11). The density of these particles is greater in the longitudinal (L) direction than in the transverse (LT) direction of the extruded plate. Figure 12 reveals the morphology of an iron-rich intermetallic identified as Al_7Cu_2Fe by SAD [38].

4.3 Tensile Properties

A compilation of the monotonic mechanical properties of the Al-Li-Cu-Mg-Zr alloy, in the longitudinal (L) and long-transverse (LT) directions is given in Tables 4 and 5. Multiple (three) samples were tested for each condition, and no significant variation between the samples was observed.

The yield strength in the transverse (LT) direction (443 MPa) is 23% lower than the corresponding value in the longitudinal (L) direction (578 MPa). The tensile strength in the LT direction (536 MPa) is 11% lower than in the longitudinal direction (600 MPa). The ductility (% elongation) in the transverse (LT) direction (8.36%) shows over 100 percent improvement than the corresponding value in the longitudinal (L) direction (3.85%). The percent reduction in area in the transverse direction (7.41%) also shows a 170 percent improvement over the corresponding value in the longitudinal direction (2.73%). The true fracture stress in the L direction (617 MPa) is marginally higher than the corresponding value in the LT direction (574 MPa). The strain hardening exponent n was determined from the monotonic stress-strain curve shown in Figure 13. The alloy exhibits greater strain hardening in the transverse direction of the extruded plate.

The elastic modulus obtained by the extensometer trace, accords well in the two directions. Barring the low ductility in the longitudinal (extrusion) direction, the alloy in the T851 temper has property combinations which are attractive for aerospace applications. A comparison of the monotonic properties of AA 8090 with other aluminum alloys (orientation: longitudinal) is made in Table 5. Variation of yield strength (MPa) with total elongation (percent) for a limited selection of aluminum alloys is made in Figure 14.

4.4 Tensile Fracture

The monotonic fracture surfaces are helpful in elucidating microstructural effects on the ductility and fracture properties of alloy 8090. Extensive fractography of the tensile samples revealed:

(a) transgranular shear failure,

(b) cracking along the grain boundaries or intergranular failure,

(c) intersubgranular failure along the subgrain boundaries, and

(d) void formation at the subgrain boundaries.

Representative fracture features of the samples from the longitudinal (L) and transverse (LT) orientations are shown in Figures 15-22.

On a macroscopic scale, tensile fracture of AA 8090-T851 in the longitudinal direction was predominantly shear. The fracture surface was oriented approximately 45 degrees to the major stress axis, following a plane of maximum shear stress (Figure 15a). Shear-type of fracture tends to minimize necking and thus the triaxial state of stress and the hydrostatic component that occurs in a necked region [39]. Consequently, void nucleation at the constituent and dispersoid particles is affected.

The intermetallics in this alloy are the iron-rich particles and the magnesium-rich insoluble phases. During plastic deformation, initiation of cracks occurs at: (i) the coarse constituent particles, (ii) at particle-matrix interfaces, and (ii) at areas of poor interparticle bonding [40]. Void initiation at these particles is dependent on the deformation modes of the matrix and the particles, and is also influenced by the stress, strain and energy criteria [41]. Void initiation at a second-phase particle occurs when the elastic energy of the particles exceeds the surface energy of the newly formed void surface. For spherical particles, the critical stress (σ) for particle cracking is given by the relationship:

$$\sigma = (6\gamma\ E/q^2 d)^{0.5} \quad . \ . \ . \ . \ . \ . \ . \ (1)$$

where γ is the surface energy, E is the stiffness, q is the stress concentration factor and d is the diameter of the particle.

While satisfaction of the above equation is a necessary condition for void nucleation, it must also be aided by stress at the particle/matrix interface in excess of the interfacial strength. When the stress reaches a critical value, void nucleation occurs by interfacial separation. The interface stress (σ_1) at a particle comprises of the applied stress (σ_a) and the normal stress from the blocked slip bands (σ_p),

$$\sigma_1 = \sigma_a + \sigma_p = \sigma_a + KF\ (r)^{0.5} \quad . \ . \ . \ . \ (2)$$

where σ_p is equated to the product of the constant K, the flow stress F, and the square root of the slip band length (r) When the interface stress exceeds the fracture strength of the particle, fracture occurs and a void is formed. Coalescence of the voids is the last stage in the fracture by dimpled rupture. Void coalescence in this alloy is governed by both void sheet formation and void impingement.

Long secondary cracks, or ledges were observed on the fracture surfaces, separating the transgranular and intergranular regions, with the crack plane oriented parallel to the loading axis which also was the extrusion direction (Figure 15b). The tendency toward localized inhomogeneous planar deformation due to the presence of ordered coherent and partially coherent matrix strengthening precipitates in lithium-containing aluminum alloys results in strain localization. For the alloy and in the aging condition (peak-aged) studied, the coarse slip bands impinge upon the grain boundaries and cause strain localization, the magnitude of which depends on the slip length. The localized planar deformation produces a large stress concentration at grain boundaries. The high stress concentration initiates voids at the coarse constituent particles, dispersoids and precipitates along the grain boundary. The linking of similar voids initiated at grain boundary precipitates results in dimpled intergranular fracture and the ledges observed on the fracture surface. The transgranular regions comprised of pronounced cracking along the sub-grain boundaries, parallel to the major stress axis (Figure 16 and 17). The transgranular fracture regions were featureless (Figure 18).

The subgrain structure in the unrecrystallized regions have a marked influence on the fracture characteristics of the quarternary alloy. The subgrains in the maximum strength, peak-aged condition are well developed. Due to low degree of misorientation between neighbouring subgrains, the impact of grain boundaries as barriers to dislocation motion is reduced. This leads to an increase in the "effective" slip length with concomitant reduction in ductility. The poor ductility of this alloy is rationalized as being not due to planar slip per se, but of its occurrence in conjunction with a strong crystallographic texture. Micro-dimples were observed on the intersubgranular fracture surface (Figure 19). These dimples are the result of the presence of the zirconium dispersoids, Al_3Zr, and the T-type ($Al_xCu_yLi_z$) precipitates. The equilibrium δ(AlLi) and Al_2MgLi phases along the high angle grain and subgrain boundaries promote intergranular microvoid coalescence. In the peak-aged condition, the increased matrix strength aids in activating the smaller dispersoids and grain boundary precipitates as void nucleating agents.

On a macroscopic scale, fracture of the transverse (LT) sample was essentially normal to the stress axis (Figure 20a). Laminar cracks were observed separating the transgranular and intergranular regions and extending down the fracture surface parallel to the loading direction (Figure 20b). The spacing between the laminar cracks is associated with fracture along grain boundaries. The tendency for intergranular failure and the sequence of events that result in necking and failure of the grains has been discussed by Srivatsan and Coyne for a ternary Al-Cu-Li alloy [41]. The lateral separation of grains which occurs under the action of triaxial stresses in plane strain, minimizes the constraints imposed by the neighbouring grains during plastic deformation. The lateral separation results in:

(i) macroscopic cracking along the recrystallized and unrecrystallized grain boundaries (Figure 21), and

(ii) microscopic cracking along the individual subgrains (Figure 22).

The fracture path along grain and subgrain boundaries is shown diagrammatically in Figure 21b and Figure 22b. The transgranular fracture regions were covered with a network of very fine dimples. These dimples are most lilkely associated with the zirconium dispersoids, Al_3Zr, the iron-rich constituents, and the equilibrium δ(AlLi), S (Al_2CuMg) and T-type ($Al_xCu_yLi_z$) precipitates.

4.5. Corrosion Testing

4.5.1 Solution Chemistry

Variation of pH level of the solution with time is exemplified in Figures 23 and 24 and reveals that for the highly acidic solutions, the pH rapidly increased during the initial hours of testing and thereafter remained more or less constant for the remaining part of the test period (test time being 21 days for 504 hours). Formation of lithium hydroxide (LiOH) and aluminum hydroxide ($Al(OH)_3$)on exposure of the alloy to the aqueous solution is responsible in part for the alkalinity and shift in pH level. The increase in pH level denotes a tendency of the solution to become alkaline and consequently, a decrease in aggressiveness of the solution.

However, for the basic solutions (pH > 7), a decrease in pH level was observed during the initial hours of testing, following which the pH level remained constant. The shift in pH level, namely, a decrease, indicates a tendency of the solution to become acidic and consequently, aggressive. A comparison of the variation of pH level of the basic solutions with time is exemplified in Figure 24.

4.5.2 Weight Loss

An insight into the general corrosion behavior of the quarternary alloy under total immersion conditions can be obtained by considering the results presented in Tables 7-13 and exemplified in Figures 25-27. These figures reveal the variation of weight loss in aqueous solutions spanning an entire range of aggressiveness.

Under total immersion conditions, weight loss occurred in all the solutions (acidic, neutral and basic) over the three week testing period. The magnitude of weight loss was directly related to the aggressiveness of the aqueous solution. The weight loss in acidic solutions (pH <7) was several times greater than the corresponding weight loss in the neutral solution (3.5 % NaCl; 0.6 N; pH 7). The weight loss in an aqueous solution of pH 1 was an order of magnitude greater than the corresponding weight loss in the neutral solution, and several times more than the corresponding weight loss in the aqueous solutions of pH 2, pH 4 and pH 5. Further, in the aqueous solution of pH 1 the weight loss of the corrosion coupons was observed to progressively increase with test time (Figure 25). However, in aqueous solutions of pH 2, pH 4 and pH 5, the weight loss data indicates that there is an initial very high rate of corrosion followed by a period where there is little further weight loss (Figure 26). The initial loss in weight results from a high corrosion rate.

During total immersion, the first stage of corrosion is associated with initiation of pits following which pit growth occurs. During pit growth there will be a high rate of corrosion with concomitant increase in weight loss [42]. Growth of the pits is inhibited by the formation of protective films and repassivation. As a result, the corrosion rate drops and there results a drastic change in weight loss.

Weight loss also occurred in the basic solutions (pH>13), the magnitude of which increased as the solution pH increased, i.e., the weight loss of the corrosion coupons in an aqueous solution of pH 13 was several times greater than the corresponding weight loss in the aqueous solution of pH 9, and an order of magnitude greater than the weight loss that occurred in the neutral solution (pH 7). Comparison of the weight loss in an acidic (pH 5), a basic (pH 9) and in the neutral solution (pH 7) is made in Figure 27, and reveals that while the weight loss progressively increased in the neutral solution, it was more or less constant after prolonged immersion in aqueous solutions of pH 5 and pH 9.

The loss in weight experienced by the Al-2.8Li-1.3Cu-0.7Mg-0.12Zr alloy coupons suggests selective attack of: (i) the active lithium-bearing phases present in the alloy, (ii) the second-phase particles dispersed in the matrix, (iii) the grain boundary precipitates, and (iv) the high angle and low angle (subgrain) boundaries. The increased weight loss observed both in the acidic and basic solutions suggests that several of these mechanisms may be operative in the hostile environments when compared to the less hostile environment, that is, the neutral solution.

4.5.3 Corrosion Rate

Variation of corrosion rate expressed in milligrams /dm^2/day (mdd) and mils per year (mpy) with test time is exemplified in Figures 28-30. The initial high corrosion rate results in a large weight loss. The apparent corrosion rates under total immersion in acidic solutions is orders of magnitude greater than the corrosion rates in the neutral solution (Figure 28) and several times more than the corrosion rates in basic solutions (Figure 29). The corrosion rate progressively decreases with time and is attributed to several concurrent and mutually-competitive factors involving:

(a) formation of thin protective films rich in carbonate and hydroxide which protects the base metal from the aggressive solution,

(b) a shift in solution pH level, and

(c) repassivation.

The apparent corrosion rate decreases with time in all the solutions, i.e., the corrosion rates are lower at 400 hours than at 50 hours. Repassivation coupled with the formation of protective films results in ceasing pit growth with concomitant reduction in corrosion rate [42,43]. Besides, the formation of lithium hydroxide (LiOH), aluminum hydroxide ($Al(OH)_3$) and lithium and copper carbonates during exposure of the alloy to the aqueous solution is responsible for alkalinity and shift in the pH levels. The tendency for the pH level of the solution to become less acidic with increased exposure time of the coupons to the solution is an appealing rationale for the progressive decrease in corrosion rate. The higher corrosion rate in acidic solutions indicates that pit initiation, growth and intergranular attack all occur and continue throughout the exposure period. The variation of corrosion rate with solution pH for different time periods is exemplified in Figure 31.

Examination of the surfaces of the corrosion coupons at both high and low magnifications by optical microscopy and scanning electron microscopy revealed the presence of pits in specimens exposed to the acidic, neutral and basic solutions. However, in solutions with high corrosion rates (solutions of pH 1 and pH 2), the surfaces underwent severe degradation especially along the grain and subgrain boundaries (Figures 32 and 33). The amount of degradation increased with increased exposure (immersion) time to the solutions (Figures 34 and 35). In corrosion coupons immersed in hostile acidic solutions, in addition to selective attack along the grain and subgrain boundaries, pitting was observed to occur at the second-phase particles dispersed in the matrix and at the grain boundary precipitates (Figure 36 and 37). High magnification examination of the pits revealed an intergranular mode of attack.

In mildly acidic solutions (pH 5), pitting at second-phase particles dispersed in the matrix and at grain boundary precipitates was far more severe than corrosion along the grain boundaries. With increased immersion time in the aqueous solution, selective attack of the grain boundary precipitates occurred resulting in the formation of pits at these sites. The number density and size of the pits increased with time of exposure to the solution Pitting took place in the neutral solution (pH 7) (Figure 39) but there was no evidence of grain boundary attack even after prolonged immersion in the solution. As the time of exposure to the solution increased, the size and number density of pits associated with matrix particles and grain boundary precipitates increased (Figure 40). In the basic solution (pH 9) pitting was found to be more dominant than attack along the grain boundaries (Figures 42 and 43). Pitting corrosion dominated and increased with immersion time or days of immersion in the solution.

SUMMARY

1. Microstructure

   * The alloy was partially recrystallized with the grains flattened and elongated in the extrusion direction of the plate. The unrecrystallized grain comprised of well-developed subgrains.

   * The grain and subgrain boundaries were decorated with particles.

2. Tensile Properties

   * The double aging treatment (32 hours at 170^{o}C (338 F) plus 40 hours at 163^{o}C (325 F) resulted in the alloy having high strength (yield strength = 578 MPa and tensile strength = 600 MPa) with total elongation of 3.85 % and reduction in area of 2.73 % in the longitudinal (extrusion) direction. The total elongation(8.36%) and reduction in area (7.41%) was an order of magnitude higher in the transverse direction of the extruded plate.

3. Fracture

   * Fracture in the maximum strength, peak-aged condition, was predominantly low energy intergranular and intersubgranular separation, with fracture associated with the subgrain boundaries.

   * The fracture process is governed by a complex interplay among several factors involving the

intrinsic microstructural features, the matrix deformation characteristics and grain boundary failure.

4. Corrosion

* Weight loss occurred in all the solutions. The weight loss in acidic solutions (pH < 7) was an order of magnitude greater than the corresponding weight loss in the neutral solution (pH 7), and several times greater than the corresponding weight loss in the basic solutions.

* The weight loss data suggests the operation of several concurrent and competing processes, namely, selective attack of: (a) the matrix strengthening precipitates, (b) the second-phase particles dispersed in the matrix, and (c) the grain boundary precipitates and corrosion along the grain boundaries. The increased weight loss observed in acidic solutions suggests that several of these mechanisms may be operative in the highly hostile acidic solution when compared to the less hostile neutral solution.

* pH level of the solutions varied during the test period. pH of the acidic and neutral solutions rapidly increased during the first few hours of testing and remained fairly constant for the major portion of the test period. For the basic

solutions, the pH decreased at first and remained more or less constant thereafter.

* Corrosion rates expressed in mils per year (mpy) and milligrams per square decimeter per day (mdd) progressively decreased with time in both the acidic and basic solutions. However, in the neutral solution, the corrosion rate was observed to increase slightly during the entire testing period.
* In highly aggressive environments there occurred:
  (a) uniform pitting at the second-phase particles dispersed in the matrix and at the grain boundary precipitates,
  (b) preferential attack of the matrix strengthening precipitates, and
  (c) enhanced corrosion along both the high angle and low angle (subgrain boundaries).

In the neutral solution, the number density and size of the pits increased with increased immersion time in the solution. In the basic solutions, uniform pitting was more dominant than corrosion along the grain boundaries.

REFERENCES

1. Aluminum-Lithium Alloys: Proceedings First International Conference on Aluminum-Lithium Alloys, T. H. Sanders, Jr., and E. A. Starke, Jr., (Eds.), Metallurgial Society of AIME, Warrendale, PA, 1981.

2. Aluminum-Lithium Alloys II: Proceedings of the Second International Conference on Aluminum-Lithium Alloys, T. H. Sanders, Jr., and E. A. Starke, Jr., (Eds.), Metallurgical Society of AIME, Warrendale, PA, 1984.

3. Aluminum-Lithium Alloys III: Proceedings of the Third International Conference on Aluminum-Lithium Alloys, C. A. Baker and P. J. Gregson (Eds.), Institute of Metals, London, 1985.

4. Aluminum Alloys, Their Physical and Mechanical Properties: Proceedings of the First International Conference on Aluminum Alloys, E. A. Starke, Jr., and T. H. Sanders, Jr., (Eds.), EMAS, U. K., 1986.

5. K. K. Sankaran and N. J. Grant: Proceedings Aluminum -Lithium Alloys I, T. H. Sanders, Jr., and E. A. Starke, Jr., (Eds.), AIME, 1981, p. 205.

6. V. Wigotsky: Aerospace America, 1984, p. 74.

7. I. M. LeBaron: U. S. Patent No. 2,381,219, Granted in 1945.

8. E. A. Starke, Jr., T. H. Sanders, Jr., and I. G. Palmer: Journal of Metals, Vol. 33, 1980, p. 24.

9. E. Ness and N. Ryum: Scripta Metallurgica, Vol. 5, 1971, p. 987.

10. J. G. Rinker, M. Marek and T. H. Sanders, Jr.: Materials Science and Engineering, Vol. 64, 1984, p. 203.

11. A. K. Vasudevan, R. C. Malcolm, W. G. Fricke and R. J. Rioja: Final Report, Contract No. N00019-80-C-0569 for the Naval Air Systems Command, June 1985.

12. L. Christoudoulou, L. Struble and J. R. Pickens: Proceedings Aluminum-Lithium Alloys I, T. H. Sanders, Jr., and E. A. Starke, Jr., (Eds.), AIME, 1984, p. 561.

13. P. P. Pizzo, R. P. Galvin and H. G. Nelson: Proceedings Aluminum-Lithium Alloys II, T. H. Sanders, Jr., and E. A. Starke, Jr., (Eds.), AIME, 1984, p. 627.

14. P. Niskanen, T. H. Sanders, Jr., M. Marek and J. G. Rinker, Jr.: Proceedings Aluminum-Lithium Alloys I, T. H. Sanders, Jr., and E. A. Starke, Jr., (Eds.), AIME, 1981. p. 347.

15. T. Magnin, C. Duberry and P. Rieux: Proceedings Aluminum Alloys: Their Physical and Mechanical Properties, E. A. Starke, Jr., and T. H. Sanders, Jr., (Eds.), EMAS, 1986, p. 177.

16. P. P. Pizzo and D. L. Daeschner: Proceedings Aluminum Alloys: Their Physical and Mechanical Properties, T. H. Sanders, Jr., and E. A. Starke, Jr., (Eds.), EMAS,1986, p. 1197.

17. J. K. Gregory, P. J. Meschter and J. E. O'Neal: Proceedings Aluminum Alloys: Their Physical and Mechanical Properties, E. A. Starke, Jr., and T. H. Sanders, Jr., (Eds.), EMAS, 1986, p. 1227.

18 R. E. Ricker and D. J. Duquette: Proceedings Aluminum -Lithium Alloys II, T. H. Sanders, Jr., and E. A. Starke, Jr., (Eds.), AIME, 1984, p. 581

19. K. R. Stokes, D. A. Moth and P. J. Sherwood: Proceedings Aluminum-Lithium Alloys III, C. A. Baker and P. J. Gregson, (Eds.), Institute of Metals, p. 294, 1985.

20. W. R. D. Jones and P. P. Das: Journal Institute of Metals, Vol 88, 1959-60, p. 435.

21. B. Noble and G. E. Thompson: Metal Science Journal, Vol. 5, 1971, p. 114

22. C. J. Peel,. B. Evans, C. A. Baker, D. A. Bennett, P. J. Gregson and H. M. Flower : Proceedings of Aluminum-Lithium Alloys II, T. H. Sanders, Jr., and E. A. Starke, Jr., (Eds.), 1984, p. 363.

23. I. G. Palmer, R. E. Lewis, D. D. Crooks, E. A. Starke, Jr., and R. E. Crooks: Proceedings Aluminum-Lithium Alloys II, T. H. Sanders, Jr., and E. A. Starke, Jr., (Eds.), 1984, p. 91.

24. W. S. Miller, A. J. Cornish, A. P. Titchener and D. A. Bennet: Proceedings Aluminum-Lithium Alloys II, T. H. Sanders, Jr., and E. A. Starke, Jr., (Eds.), 1984, p. 335.

25. R. E. Crooks and E. A. Starke, Jr.: Metallurgical Transactions, Vol. 15A, 1984, p. 1367.

26. P. J. Gregson, H. M. Flower, C. N. J. Tite and A. K. Mukhopadhyay: Materials Science and Technology,

Vol. 2, 1986, p. 349.

27. P. J. Gregson and H. M. Flower: Proceedings Aluminum -Lithium Alloys III, C. A. Baker (Ed.), 1985, p. 423.

28. G. E. Thompson and B. Noble: Journal of Institute of Metals, Vol. 101, 1973, p. 111.

29. B. Noble and G. E. Thompson: Metal Science Journal, Vol. 6, 1972, p. 167.

30. J. C. Williams and E. A. Starke, Jr.: Deformation Processing and Structure, George Krause (Ed.), ASM, Metals Park, OH, 1983, p. 279.

31. R. F. Ashton, D. S. Thompson, E. A. Starke, Jr., and F. S. Lin: Ref. [3], 1985, p.66.

32. E. A. Starke, Jr., and T. H. Sanders, Jr.: Ref. [2], 1984, p. 1.

33. J. M. Silcock: Journal Institute of Metals, Vol. 88, 1959-60, p. 357.

34. T. S. Srivatsan, E. J. Coyne, Jr.,. and E. A. Starke, Jr.: Journal of Materials Science, Vol. 21, 1986, p. 1553.

35. F. S. Lin, S. B. Chakrabortty and E. A. Starke, Jr.: Metallurgical Transactions, Vol. 13A, 1982, p. 401.

36. T. S. Srivatsan and E. J. Coyne, Jr.: Aluminium, Vol. 62, 1986, p. 437.

37. D. Halliday and R. Resnick: Fundamentals of Physics, John Wiley and Sons, Inc., New York., NY, 1970.

38. A. Munity, A. Zangvil and M. Metzger: Metallurgical Transactions, Vol. 12A, 1980, p. 1863.

39. W. X. Feng, F. S. Lin and E. A. Starke, Jr.: Metallurgical Transactions, Vol. 15A. 1984, p.

40. T. S. Srivatsan, E. J. Coyne, Jr., and E. A. Starke, Jr.: Microstructural Science: Volumne 14, Proceedings of the Annual Meeting of the International Metallographic Society, M. R. Louthan, Jr, C. Bagnall and G. Vander Voort, (Eds.), 1985, p. 315.

41. T. S. Srivatsan and E. J. Coyne, Jr.: Materials Science and Technology, Vol. 3, February 1987, p. 130.

42. P. J. Lane, J. A. Gray and C. J. Smith: Proceedings of Aluminum-Lithium Alloys III, C. Baker (Ed.), Institute

of Metals, 1985, p. 273.

43. J. G. Craig, N. J. H. Holroyd, M. R. Jarrett and R. C. Newman: Proceedings of Third International Conference on Environmental Degradation of Engineering Materials, M. R. Louthan , Jr., and R. P. McNitt, (Eds.), 1987.

TABLE 1. Phases encountered in the Al-Li-Cu-Mg-Zr alloy system

Phase	Composition	Crystal Structure	Orientation Relationship
δ'	Al_3Li	$L1_2$	cube-cube
δ	AlLi	B_{32} (cubic)	$(001)_\delta \parallel (111)_\alpha$; $(100)_\delta \parallel (110)_\alpha$
Θ'	Al_2Cu	tetragonal	$(001)_{\Theta'} \parallel (001)_\alpha$; $[100]_{\Theta'} \parallel [100]_\alpha$
T_1	Al_2CuLi	hexagonal	$(0001)_{T_1} \parallel (111)_\alpha$;$[10\bar{1}0]_{T_1} \parallel [1\bar{1}0]_\alpha$
T_B	$Al_{15}Cu_8Li_2$	cubic	$(001)_{T_B} \parallel (001)_\alpha$; $[110]_{T_B} \parallel [100]_\alpha$
T_2	Al_6CuLi_3	icosahedral	unknown
β'	Al_3Zr	$L1_2$	cube-cube
S'	Al_2CuMg	orthorhombic	$[100]_{S'} \parallel [100]_\alpha$; $[010]_{S'} \parallel [021]_\alpha$

TABLE 2.

COMPOSITION OF ALUMINUM ALLOY 8090

Element	Li	Cu	Mg	Zr*	Fe	Si	Zn	Ti	Mn	Ga	Cr	Al
Amount (wt.%)	2.8	1.3	0.7	0.12	0.05	0.02	0.03	0.03	0.002	0.003	0.0005	Bal.

* Grain refiner, present as Al_3Zr.

TABLE 3
NOMINAL COMPOSITION AND DENSITIES OF SOME

ALUMINUM ALLOYS

Al-5.5Zn-2.5Mg-1.5Cu-0.3Cr	7075	2.81	g/cc
Al-4.5Cu-1.5Mg-0.6Mn	2024	2.77	g/cc
Al-4.5Cu-1.2Li-0.5Mn-0.21Cd	2020	2.71	g/cc
Al-2.9Cu-2.2Li-0.12Zr	2090	2.61	g/cc
Al-3.0Cu-1.6Li-0.79Mg-0.2Zr		2.64	g/cc
Al-1.3Cu-2.8Li-0.7Mg-0.12Zr	8090	2.50	g/cc

TABLE 4.

LONGITUDINAL MECHANICAL PROPERTIES OF ALUMINUM ALLOY 8090*

Temper	Elastic# Modulus (GPa)	0.2% Offset Yield Strength (MPa)	Tensile Strength (MPa)	YS/UTS	Percent Elong.	Percent R.A.	True Fracture Stress (MPa)	n
T851	82.77	578	600	0.96	3.85	2.73	617	0.066

* results are the mean based on Three tests

R.A. is the reduction in area

True fracture stress is defined as (σ_f/A_f)

n is the strain hardening exponent

\# Tangency measurement from extensometer trace. Accurate to $\pm$ 5 GPa

TABLE 5.

LONG TRANSVERSE MECHANICAL PROPERTIES OF ALUMINUM ALLOY 8090*

Temper	Elastic# Modulus (GPa)	0.2% Offset Yield Strength (MPa)	Tensile Strength (MPa)	YS/UTS	Percent Elong.	Percent R.A.	True Fracture Stress (MPa)	n
T851	82.80	443	536	0.83	3.36	7.41	574	0.087

* results are mean based on Three tests

R. A. is the reduction in area

True fracture stress is defines as (σ_f/A_f)

n is the strain hardening exponent

\# Tangency measurement based on extensometer trace. Accurate to $\pm$ 5 GPa.

TABLE 6.

COMPARISON OF MONOTONIC PROPERTIES OF ALLOY 8090 WITH

OTHER ALUMINUM ALLOYS

Alloy	Temper	Elastic Modulus (GPa)	Yield Strength (MPa)	Ultimate Strength (MPa)	Elong. (%)
Aluminum* (96%)	-	-	30	70	43.0
2020	T651	77	526	567	5.0
2090	T851	79	485	533	10.0
8090	T851	83	578	600	3.85
2024	T851	72	450	485	6.0
7075	T651	71	505	570	11.0

* from Aluminum by J. E. Hatch

TABLE 7. General Corrosion Results of Aluminum Alloy 8090 under Total Immersion in Solution of pH 1.

Specimen No.	Specimen Area (cm^2)	Total Immersion (days)	Weight Loss (gram)	Corrosion Rate	
				m.d.d	m.p.y
1-1	24.41	3	0.340	464.0	267.0
1-3	24.01	5	0.463	386.0	222.0
1-2	24.01	7	0.461	273.0	157.0
1-4	24.44	10	0.565	231.0	133.0
1-5	24.54	15	0.617	167.0	96.0

TABLE 8. General Corrosion Results of Aluminum Alloy 8090 under Total Immersion in Solution of pH 2.

Specimen No.	Specimen Area (cm^2)	Total Immersion (days)	Weight Loss (gram)	Corrosion Rate	
				m.d.d	m.p.y
5-1	23.99	3	0.050	69.6	40.0
5-2	23.64	7	0.060	36.3	20.9
5-3	24.02	10	0.071	29.6	17.0
5-4	23.99	15	0.074	20.3	11.7
5-5	24.07	21	0.084	16.6	9.6

TABLE 9. General Corrosion Results of Aluminum Alloy 8090 under Total Immersion in Solution of pH 4.

Specimen No.	Specimen Area (cm^2)	Total Immersion (days)	Weight Loss (gram)	Corrosion Rate	
				m.d.d	m.p.y
6-1	24.46	3	0.032	43.5	25.0
6-2	23.87	7	0.044	26.3	15.1
6-3	24.02	10	0.046	19.2	11.0
6-4	23.93	15	0.045	12.5	7.2
6-5	23.92	[illegible]	0.049	9.8	5.6

TABLE 10. General Corrosion Results of Aluminum Alloy 8090 under Total Immersion in Solution of pH 5.

Specimen No.	Specimen Area (cm^2)	Total Immersion (days)	Weight Loss (gram)	Corrosion Rate	
				m.d.d	m p.y
8-1	28.29	3	0.009	10.6	6.1
8-2	31.85	8	0.022	8.6	5.0
8-3	29.06	10	0.024	8.3	4.8
8-4	28.20	15	0.027	6.4	3.7
8-5	28.37	21	0.029	4.9	2.8

TABLE 11. General Corrosion Results of Aluminum Alloy 8090 under Total Immersion in Solution of pH 7.

Specimen No.	Specimen Area (cm^2)	Total Immersion (days)	Weight Loss (gram)	Corrosion Rate m.d.d	m.p.y
4-1	23.84	5	0.003	2.5	1.5
4-2	24.49	7	0.009	5.3	3.0
4-3	23.98	10	0.012	5.0	2.9
4-4	24.52	15	0.019	5.2	3.0
4-5	24.40	21	0.032	6.3	3.6

TABLE 12. General Corrosion Results of Aluminum Alloy 8090 under Total Immersion in Solution of pH 9.

Specimen No.	Specimen Area (cm^2)	Total Immersion (days)	Weight Loss (gram)	Corrosion Rate	
				m.d.d	m.p.y
7-1	23.42	3	0.019	27.0	15.6
7-2	24.44	7	0.029	17.0	9.8
7-3	23.95	10	0.032	13.4	7.7
7-4	24.32	15	0.031	8.2	4.7
7-5	24.46	21	0.031	6.0	3.5

TABLE 13. General Corrosion Results of Aluminum Alloy 8090 under Total Immersion in Solution of pH 13

Specimen No.	Specimen Area (cm^2)	Total Immersion (days)	Weight Loss (gram)	Corrosion Rate m.d.d	m.p.y
10-1	29.22	3	0.290	331.0	190.0
10-2	30.33	8	0.340	140.0	80.6
10-3	29.45	10	0.293	99.5	57.2
10-4	30.26	15	0.325	71.6	41.2
10-5	29.14	21	0.324	53.0	30.4

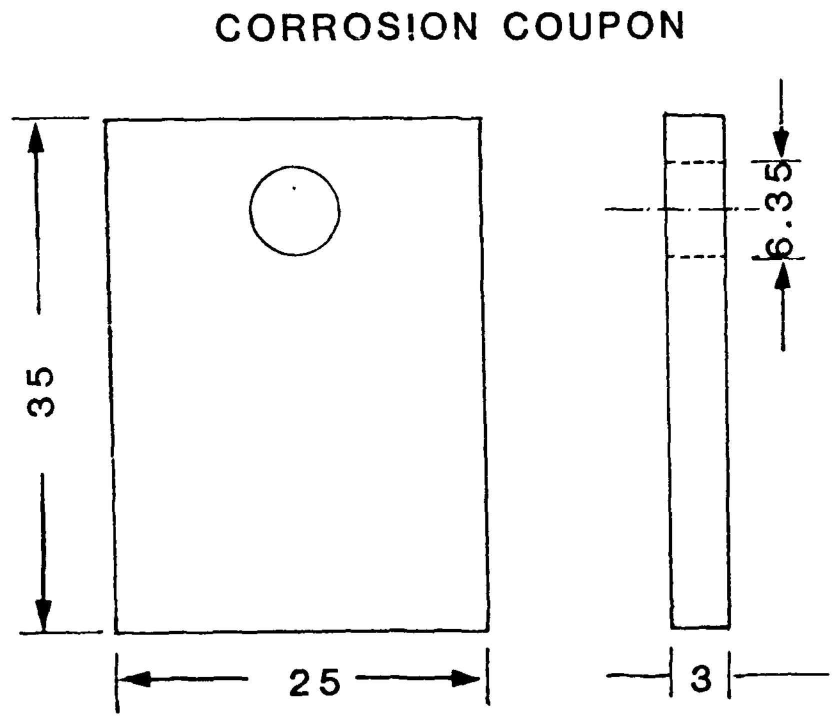

Figure 1. Schematic showing dimensions of the corrosion coupon.

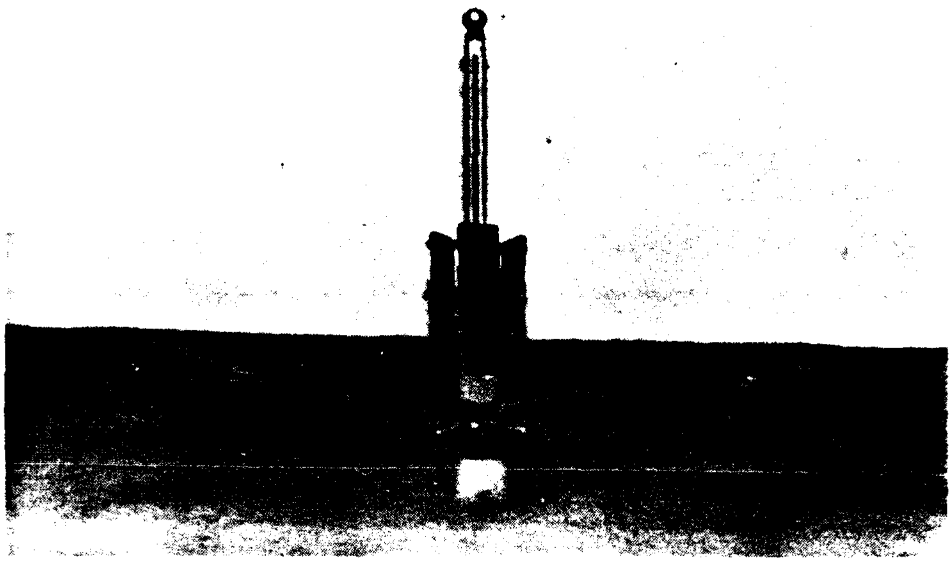

FIGURE 2. CORROSION COUPONS MOUNTED ON A GLASS STAND

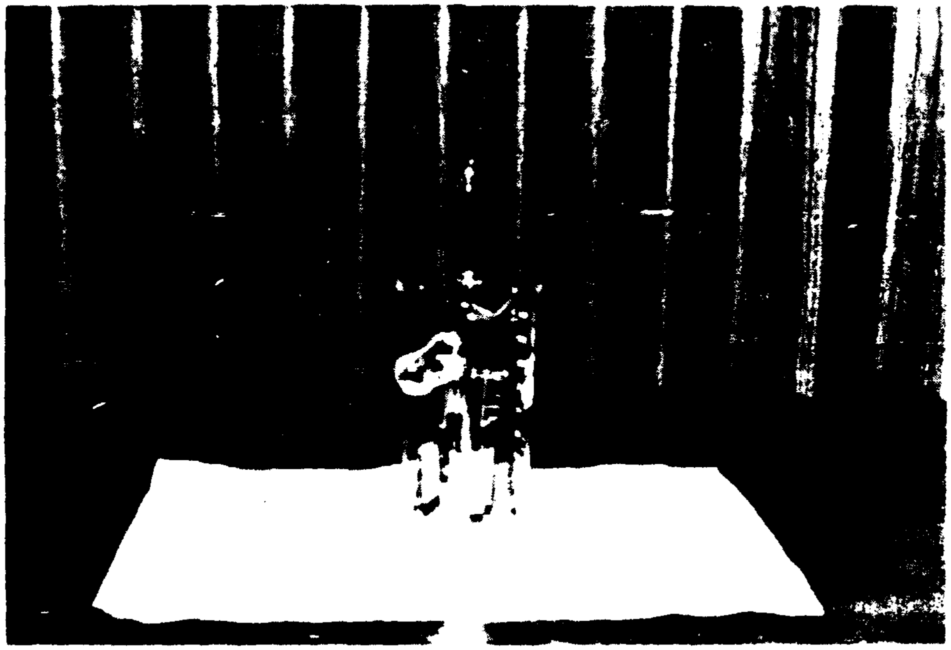

FIGURE 3. GLASS STAND WITH CORROSPON COUPONS IMMERSED IN A BEAKER CONTAINING SOLUTION OF DESIRED pH

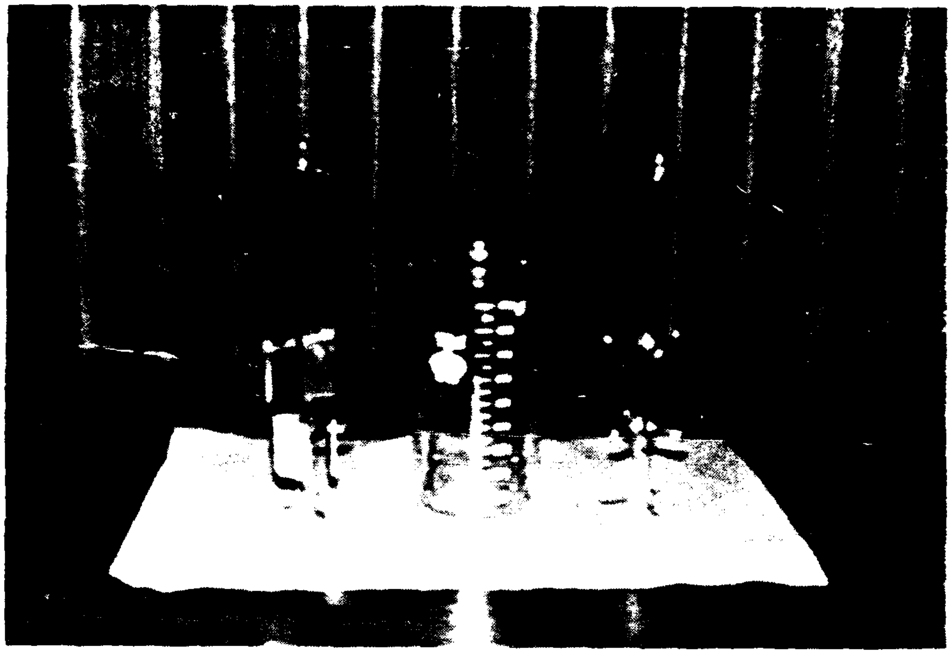

FIGURE 4. APPARATUS FOR CORROSION TESTING: CORROSION COUPONS, BEAKER AND CLASS STAND

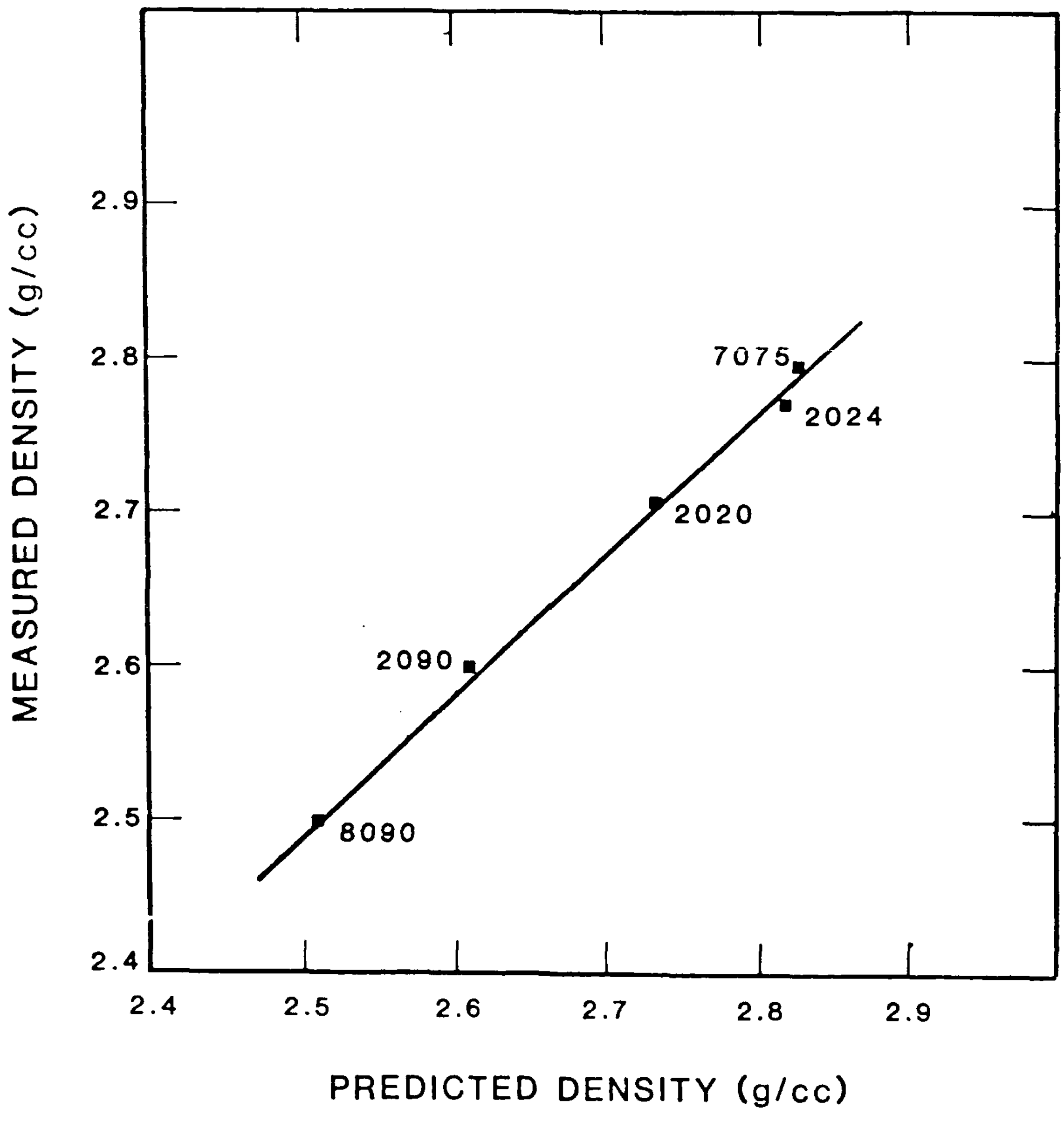

Figure 5. Density of aluminum alloy 8090 measured by hydrostatic weighing and predicted from composition; compared with a limited selection of aluminum alloys.

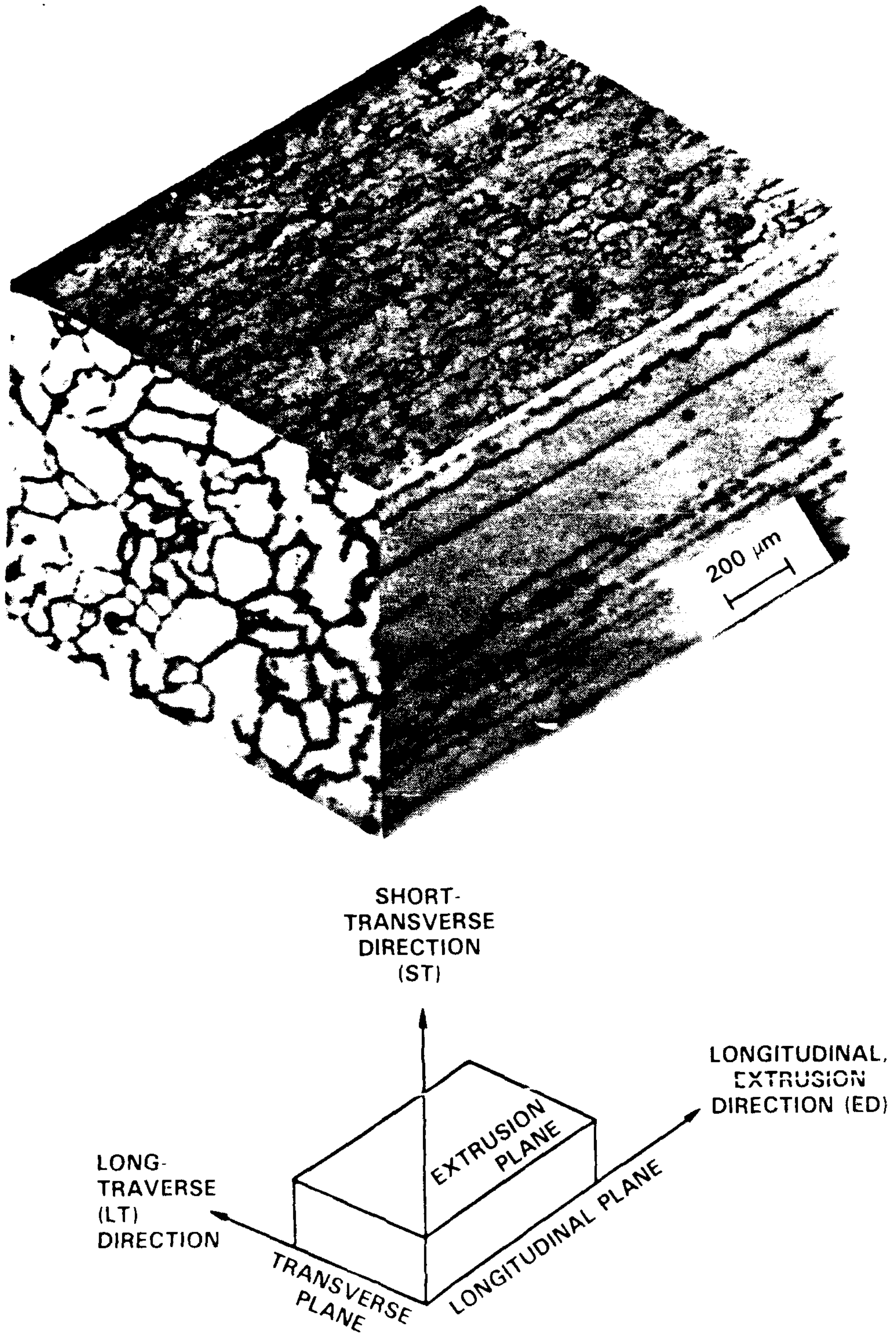

FIGURE 6. TRIPLANAR OPTICAL MICROGRAPH ILLUSTRATING GRAIN SIZE AND MORPHOLOGY OF AA 8090 EXTRUDED PLATE (KELLER'S ETCH: 90 SECONDS)

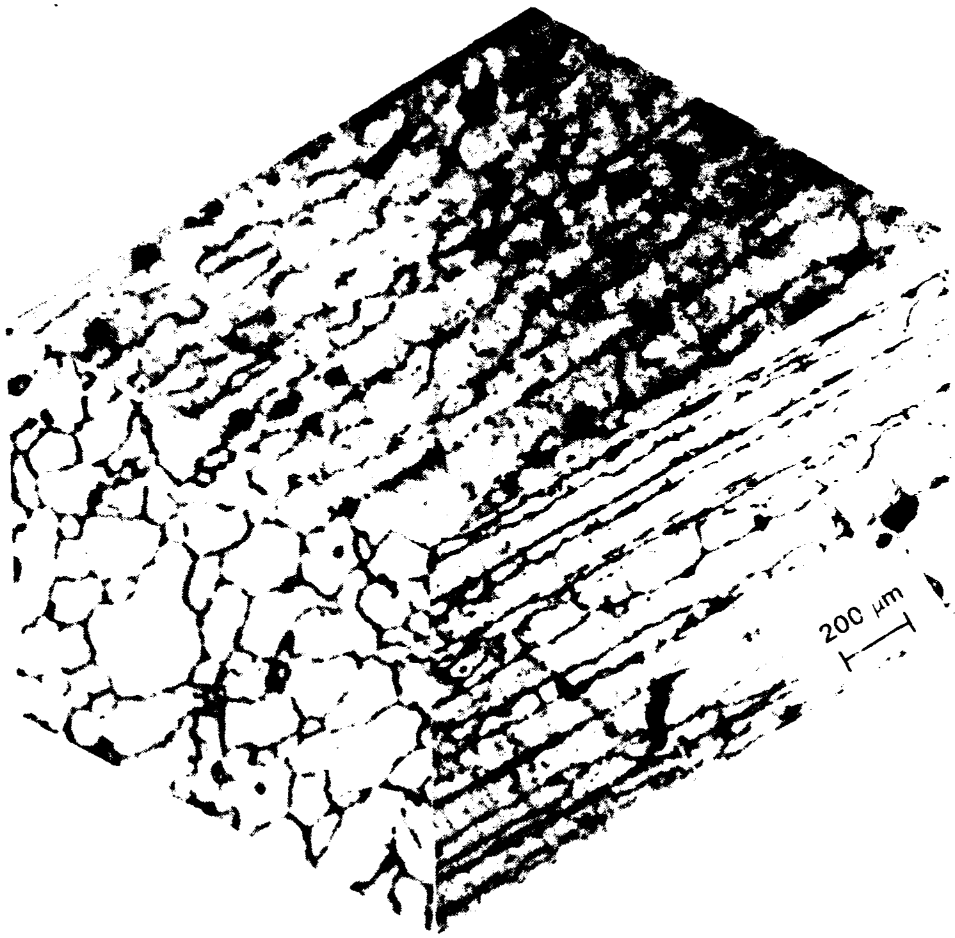

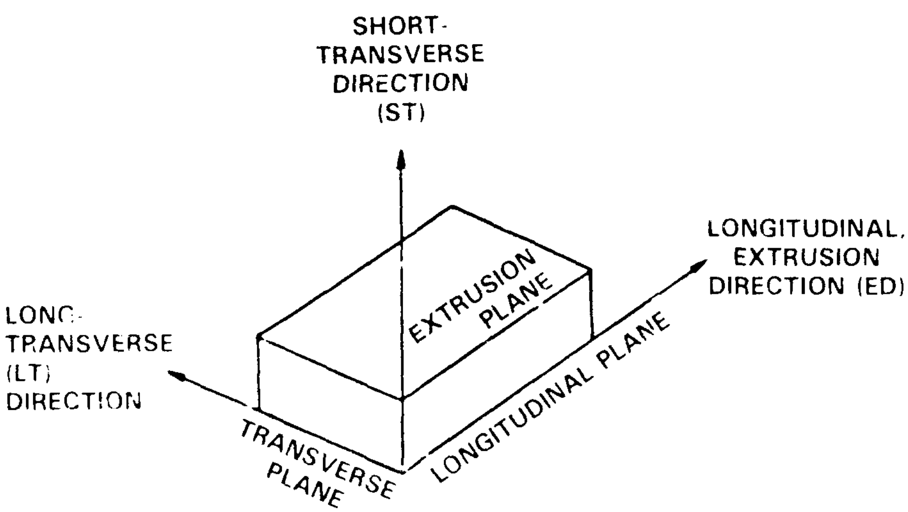

FIGURE 7 TRIPLANAR OPTICAL MICROGRAPH ILLUSTRATING THE GRAIN STRUCTURE, SIZE AND DISTRIBUTION OF SOLUBLE PHASES (10% ORTHOPHOSPHORIC ACID AT 50°C)

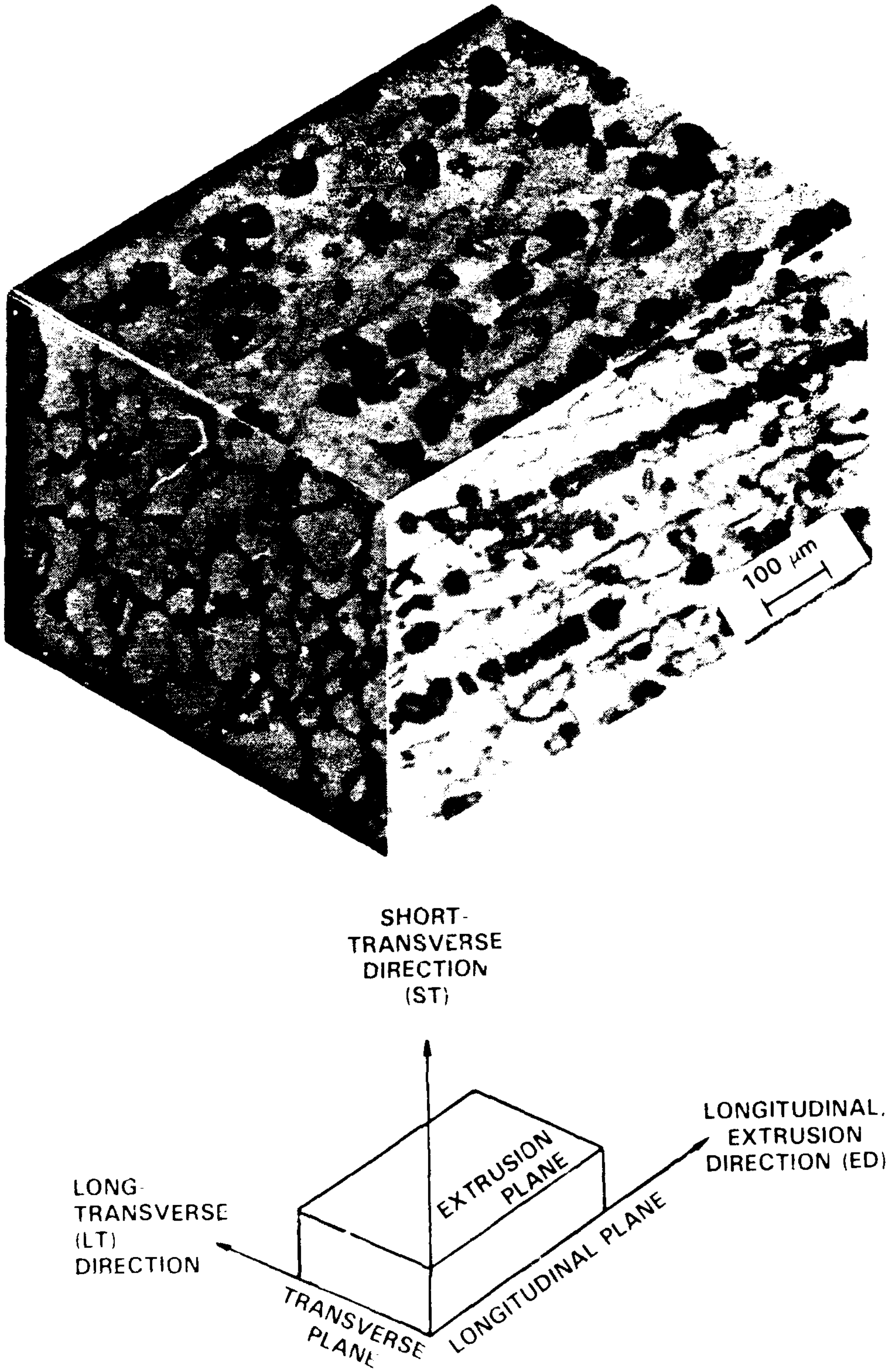

FIGURE 8. OPTICAL MICROGRAPH ILLUSTRATING PARTICLE DENSITY AND DISTRIBUTION ALONG THE THREE ORTHOGONAL DIRECTIONS OF THE EXTRUDED PLATE (KELLER'S ETCH)

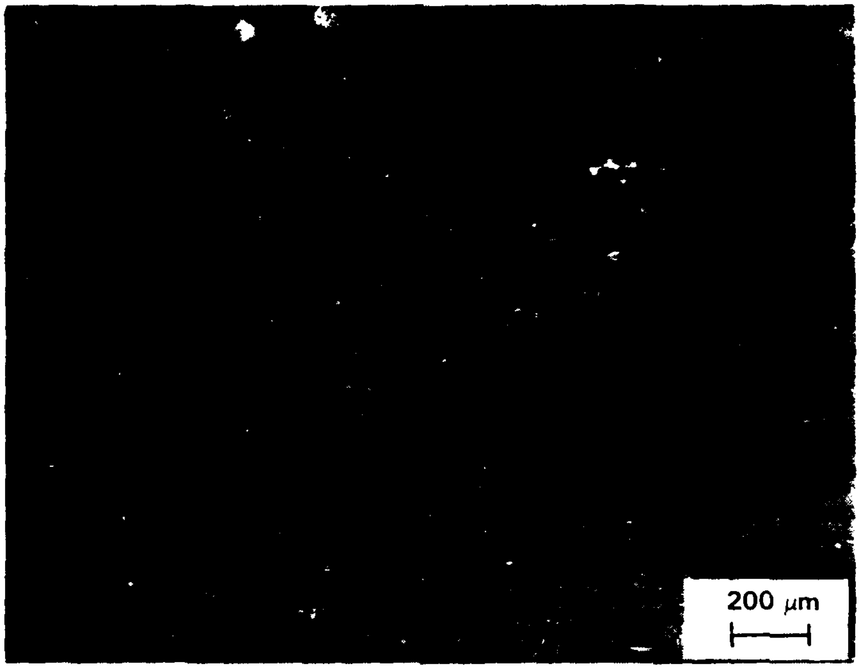

FIGURE 9. OPTICAL MICROGRAPH SHOWING GRAIN STRUCTURE ON THE SURFACE OF THE EXTRUDED PLATE, LONGITUDINAL DIRECTION

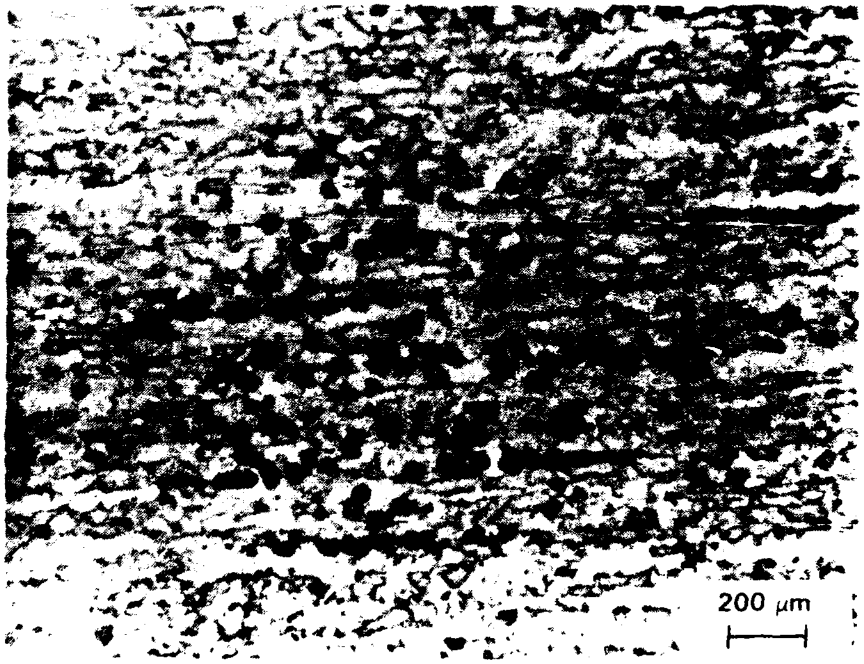

FIGURE 10. OPTICAL MICROGRAPH SHOWING "CLUSTERING" OF THE INTERMETALLIC PARTICLES – EXTRUSION DIRECTION OF THE 8090 PLATE

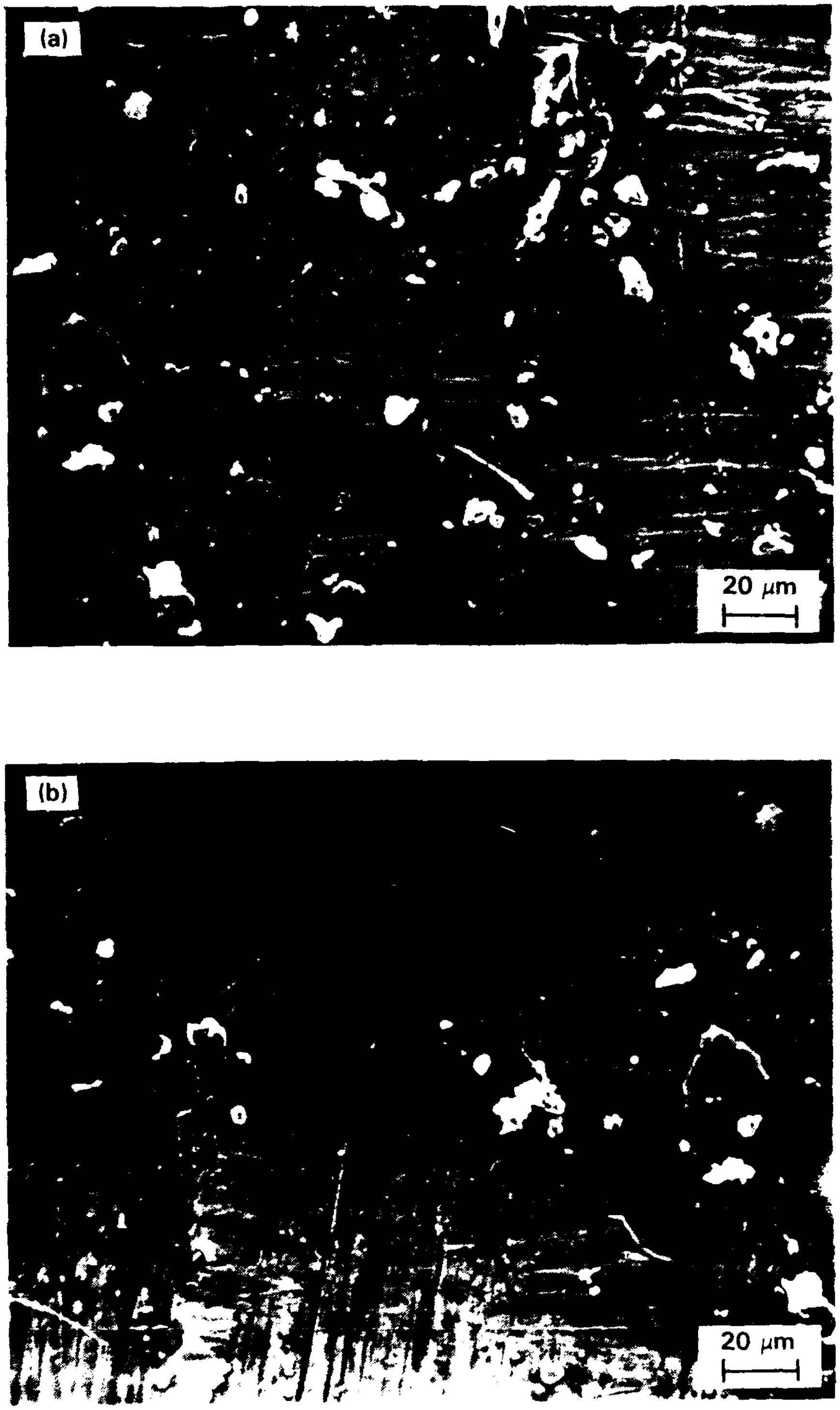

FIGURE 11. SCANNING ELECTRON MICROGRAPH SHOWING DISTRIBUTION OF PARTICLES (IRON-, SILICON- AND MAGNESIUM-RICH INTERMETALLICS) ON BROMINE-ETCHED SURFACE OF THE ALLOY: (a) LONGITUDINAL (EXTRUSION) DIRECTION, AND (b) LONG-TRANSVERSE DIRECTION

FIGURE 12. SCANNING ELECTRON MICROGRAPH SHOWING MORPHOLOGY OF IRON-RICH INTERMETALLIC (Al_7Cu_2Fe) ON BROMINE-ETCHED SURFACE (T851 CONDITION)

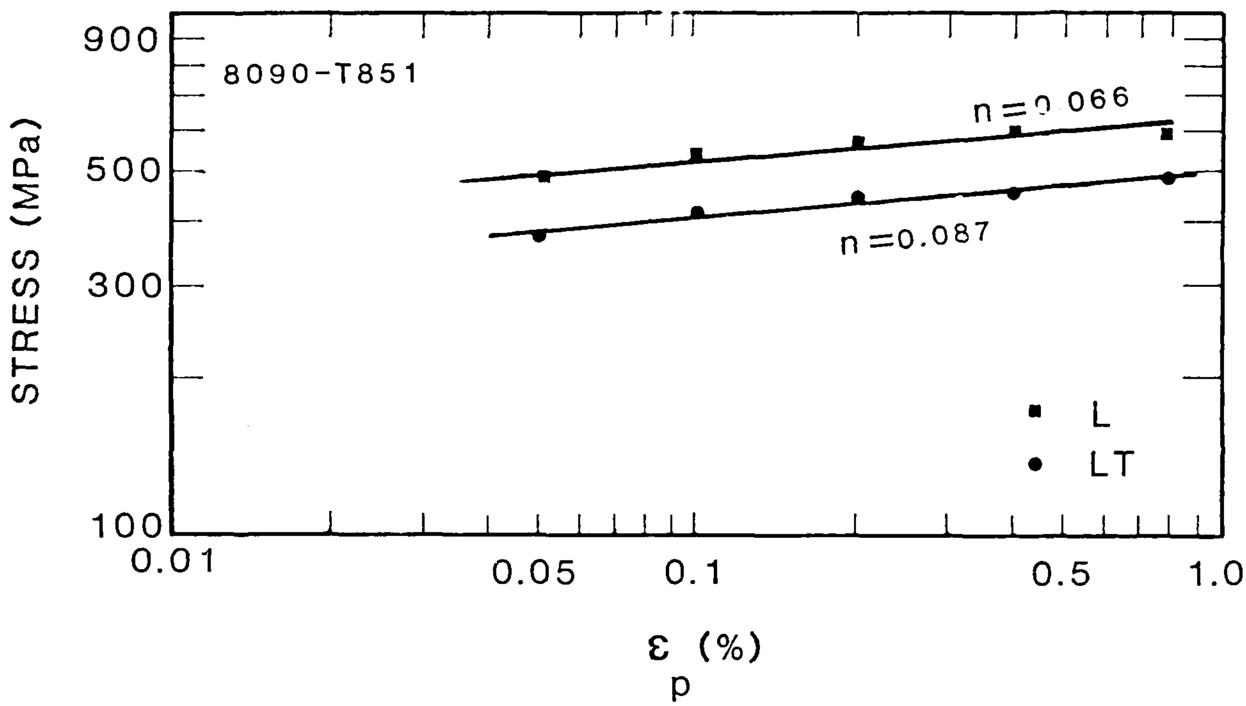

Figure 13. Monotonic stress-strain curve for alloy 8090 (T851 condition) in the longitudinal and transverse directions.

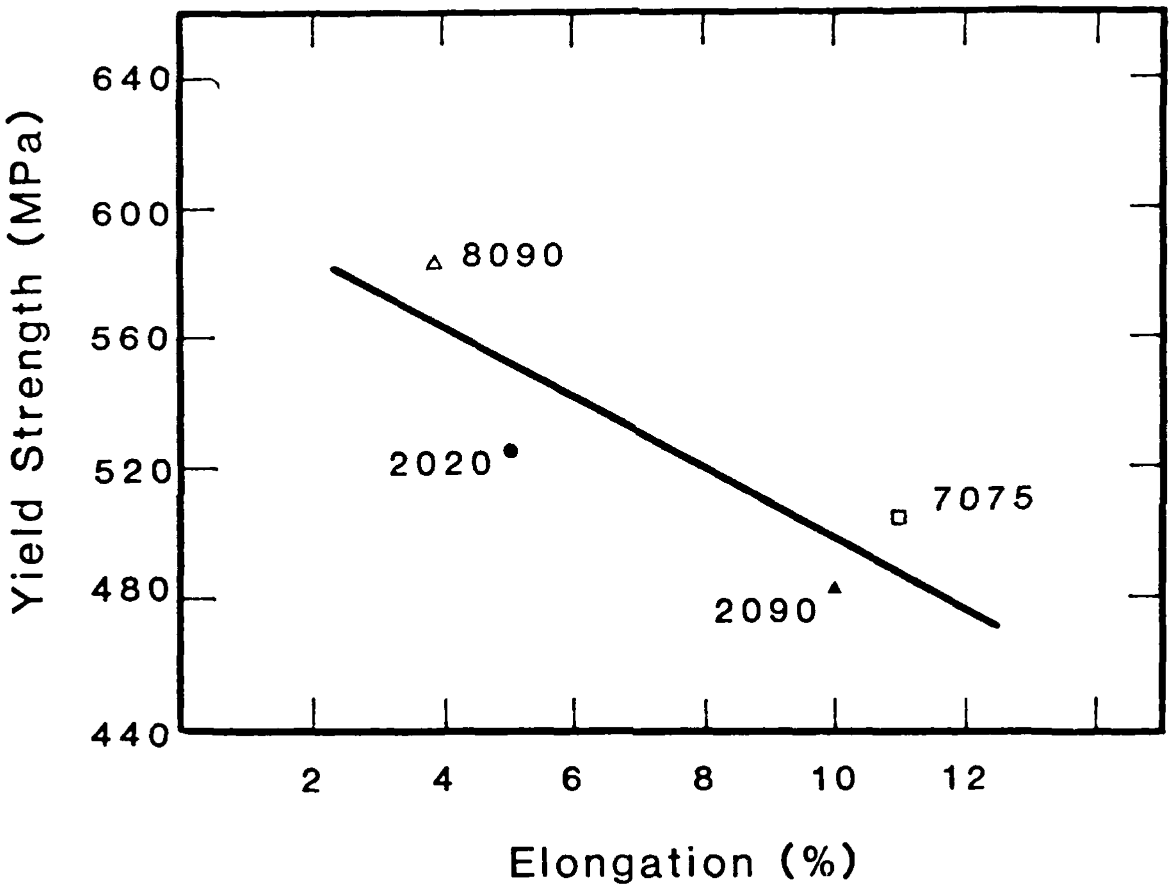

Figure 14. Comparison of yield strength versus elongation of alloy 8090 with a limited selection of aluminum alloys.

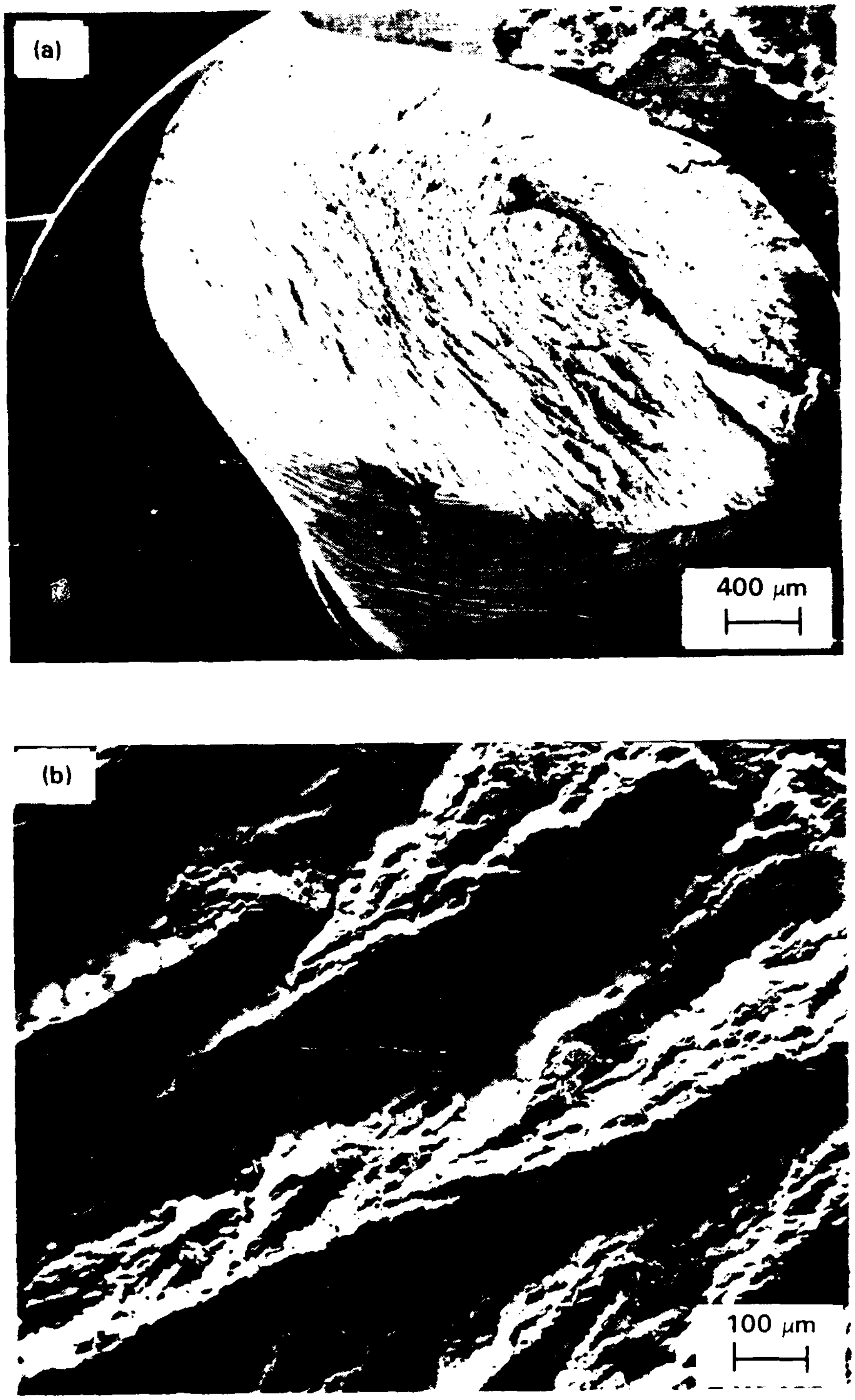

FIGURE 15. SCANNING ELECTRON MICROGRAPHS OF FRACTURE SURFACE OF THE LONGITUDINAL TENSILE SAMPLE SHOWING: (a) SHEAR-TYPE FRACTURE, AND (b) HIGH MAGNIFICATION SHOWING LARGE SECONDARY CRACKS OR LEDGES PARALLEL TO THE EXTRUSION DIRECTION.

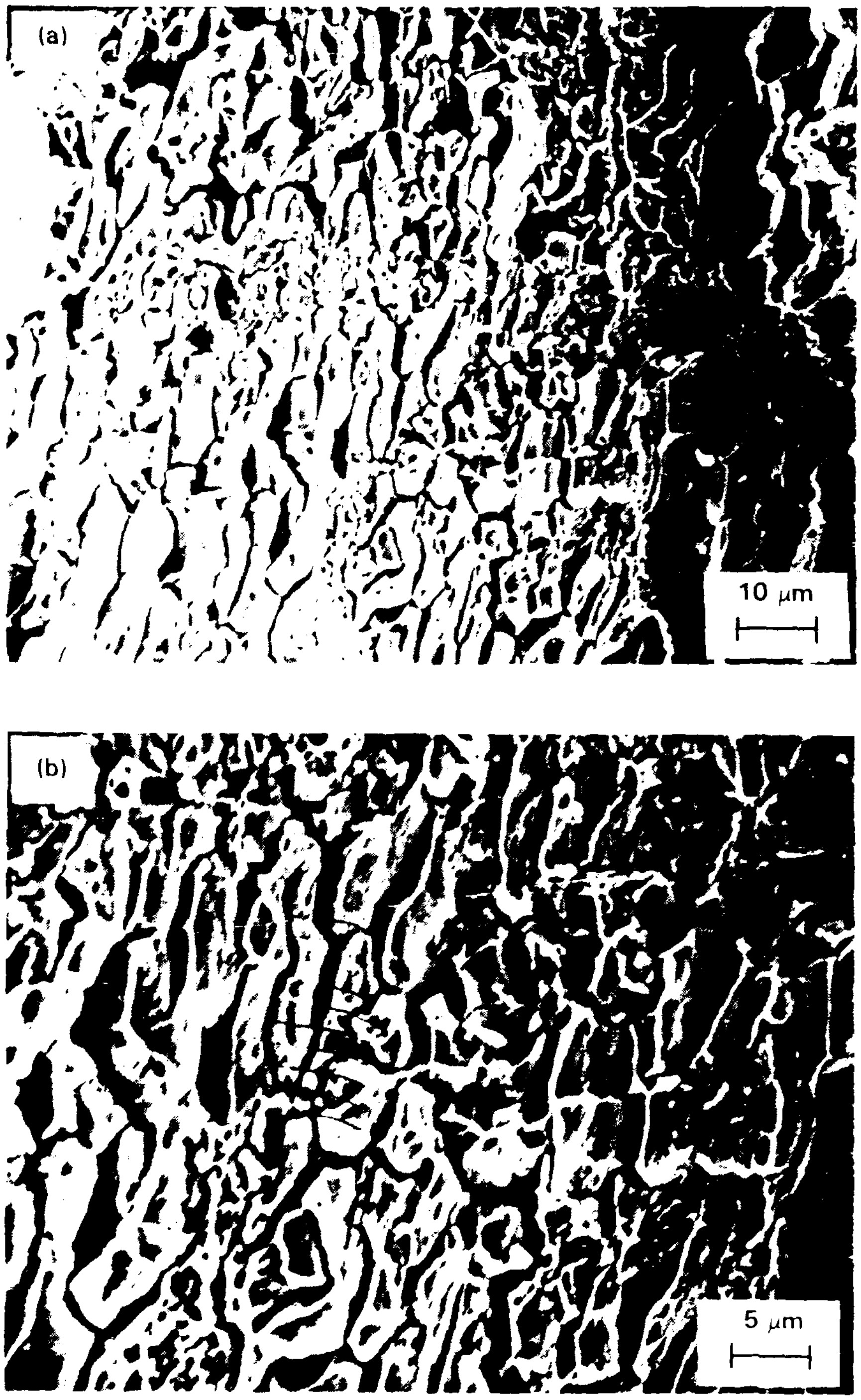

FIGURE 16 FRACTOGRAPHS OF THE LONGITUDINAL TENSILE SAMPLE SHOWING: (a) TRANSGRANULAR REGION WITH FRACTURE ALONG SUBGRAIN BOUNDARIES, AND (b) HIGH MAGNIFICATION OF (a)

FIGURE 17. HIGH MAGNIFICATION FRACTOGRAPH SHOWING CRACKING ALONG THE SUBGRAIN BOUNDARIES WITHIN THE LARGE UNRECRYSTALLIZED GRAINS

FIGURE 18. HIGH MAGNIFICATION FRACTOGRAPH OF THE LONGITUDINAL TENSILE SAMPLE OFAA 8090 SHOWING FINE INTERGRANULAR CRACKING ALONG THE SUBGRAIN BOUNDARIES, AND FEATURES OF THE TRANSGRANULAR REGION

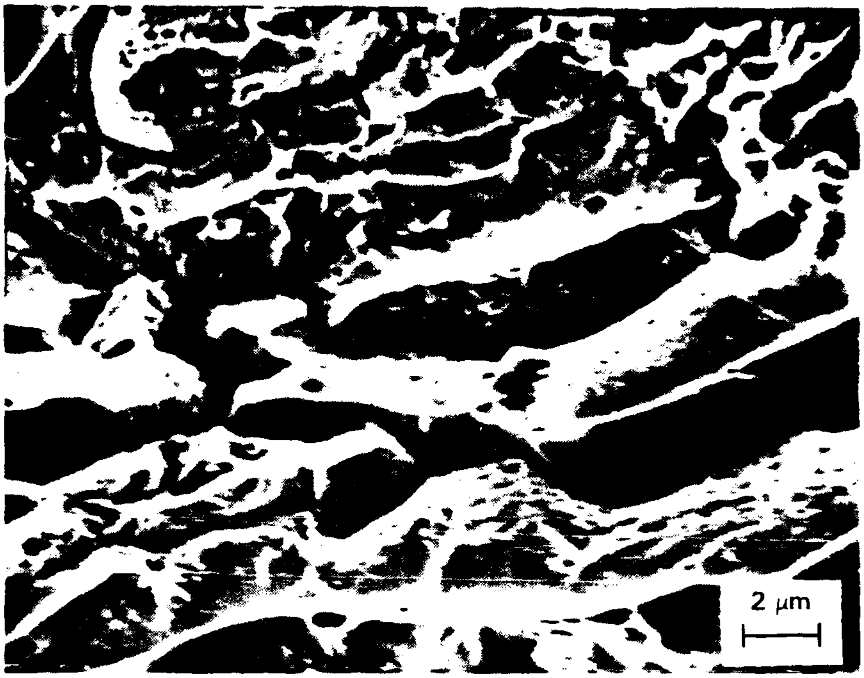

FIGURE 19. HIGH MAGNIFICATION FRACTOGRAPH SHOWING INTERGRANULAR REGIONS COVERED WITH DUCTILE DIMPLES

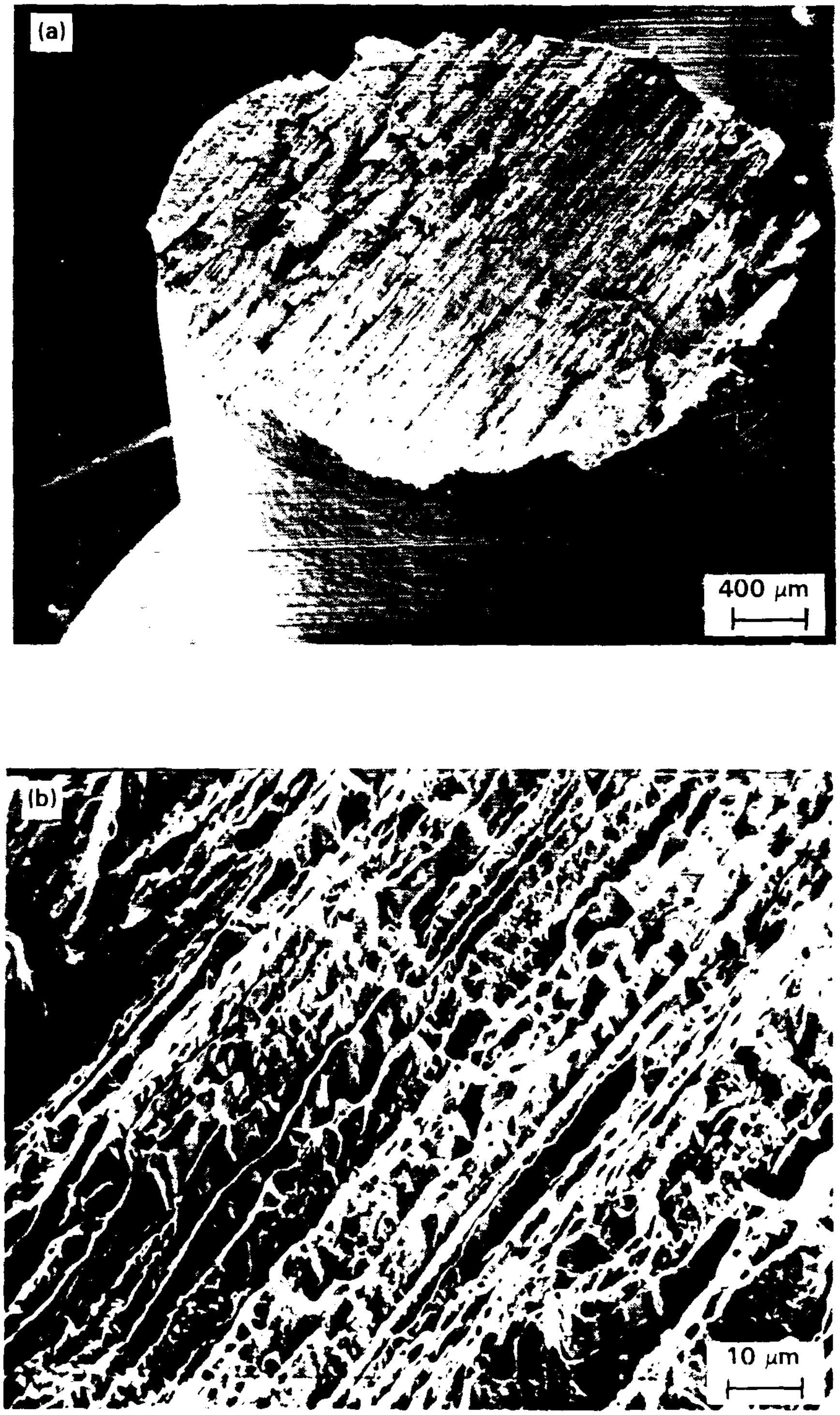

FIGURE 20. SEM OF FRACTURE SURFACE OF THE TRANSVERSE TENSILE SAMPLE SHOWING. (a) FRACTURE NORMAL TO THE STRESS AXIS, AND (b) LAMINAR CRACKS PARALLEL TO THE MAJOR STRESS AXIS, T851 CONDITION

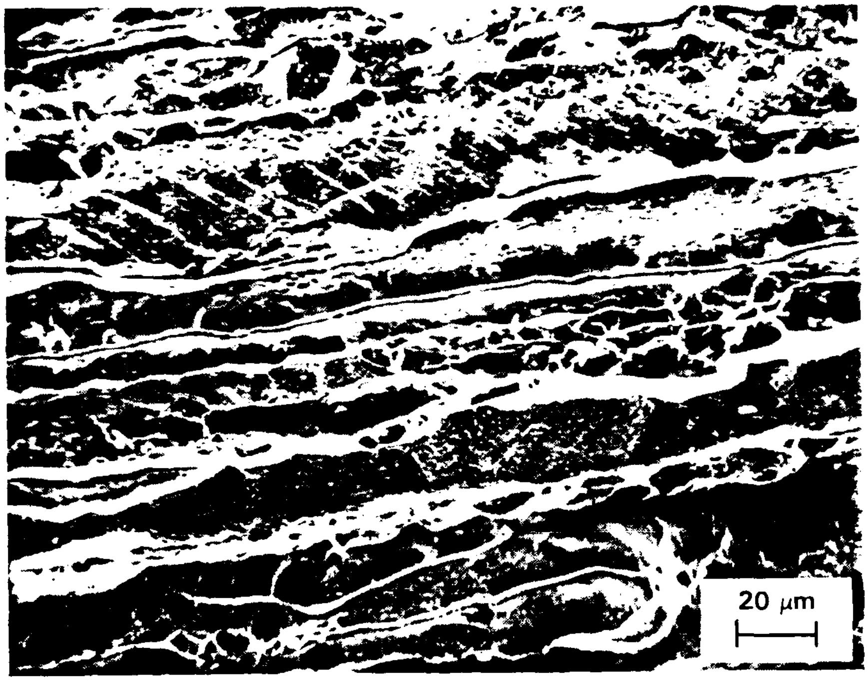

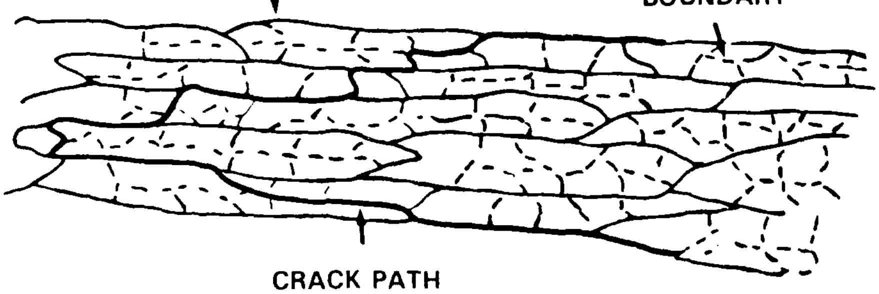

FIGURE 21. (a) HIGH MAGNIFICATION FRACTOGRAPH SHOWING INTERGRANULAR CRACKING ALONG THE LARGE UNRECRYSTALLIZED GRAIN BOUNDARIES WITH DUCTILE DIMPLES ON THE TRANSGRANULAR FRACTURE SURFACE.
(b) SCHEMATIC SHOWING MODE OF FAILURE ALONG THE LARGE UNRECRYSTALLIZED GRAIN BOUNDARIES OF AA 8090.

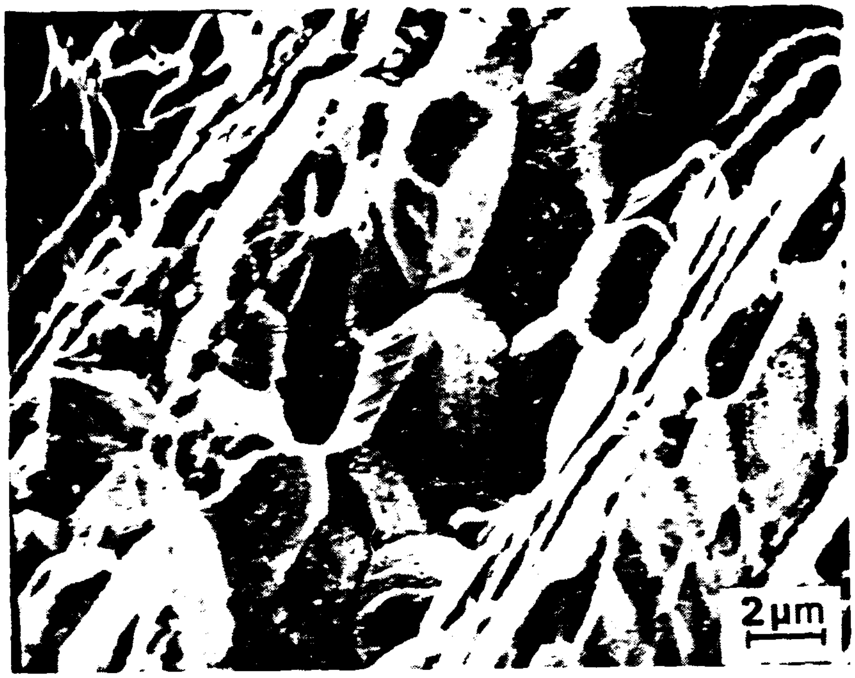

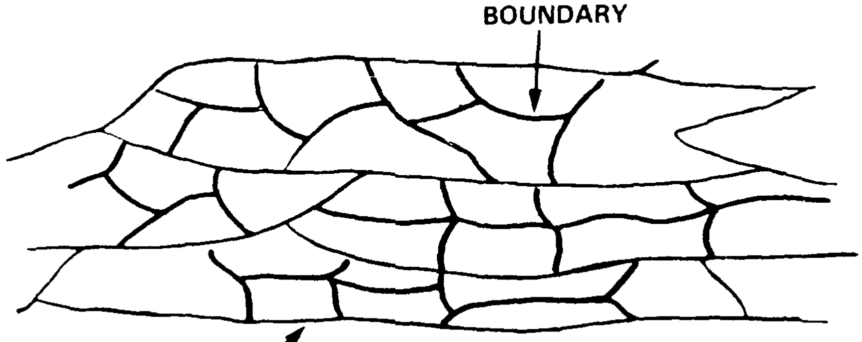

FIGURE 22. (a) FRACTOGRAPH OF RIDGE SHOWING INTERGRANULAR CRACKING ALONG THE SUBGRAIN BOUNDARIES. (b) SCHEMATIC SHOWING INTERGRANULAR CRACKING ALONG SUBGRAINS WITHIN AN UNRECRYSTALLIZED GRAIN

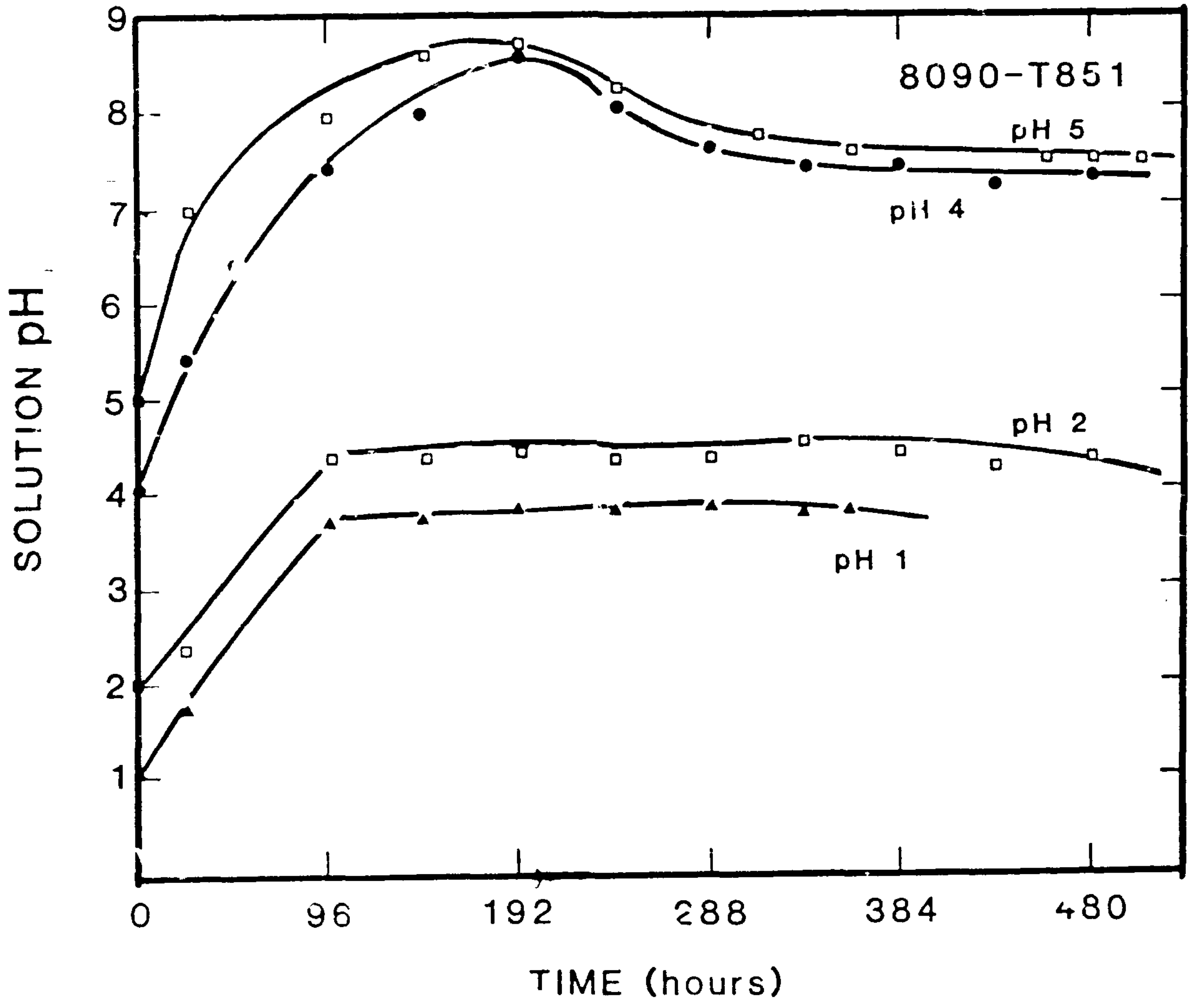

Figure 23. Comparison of the variation of solution pH of the acidic solutions with time (hours).

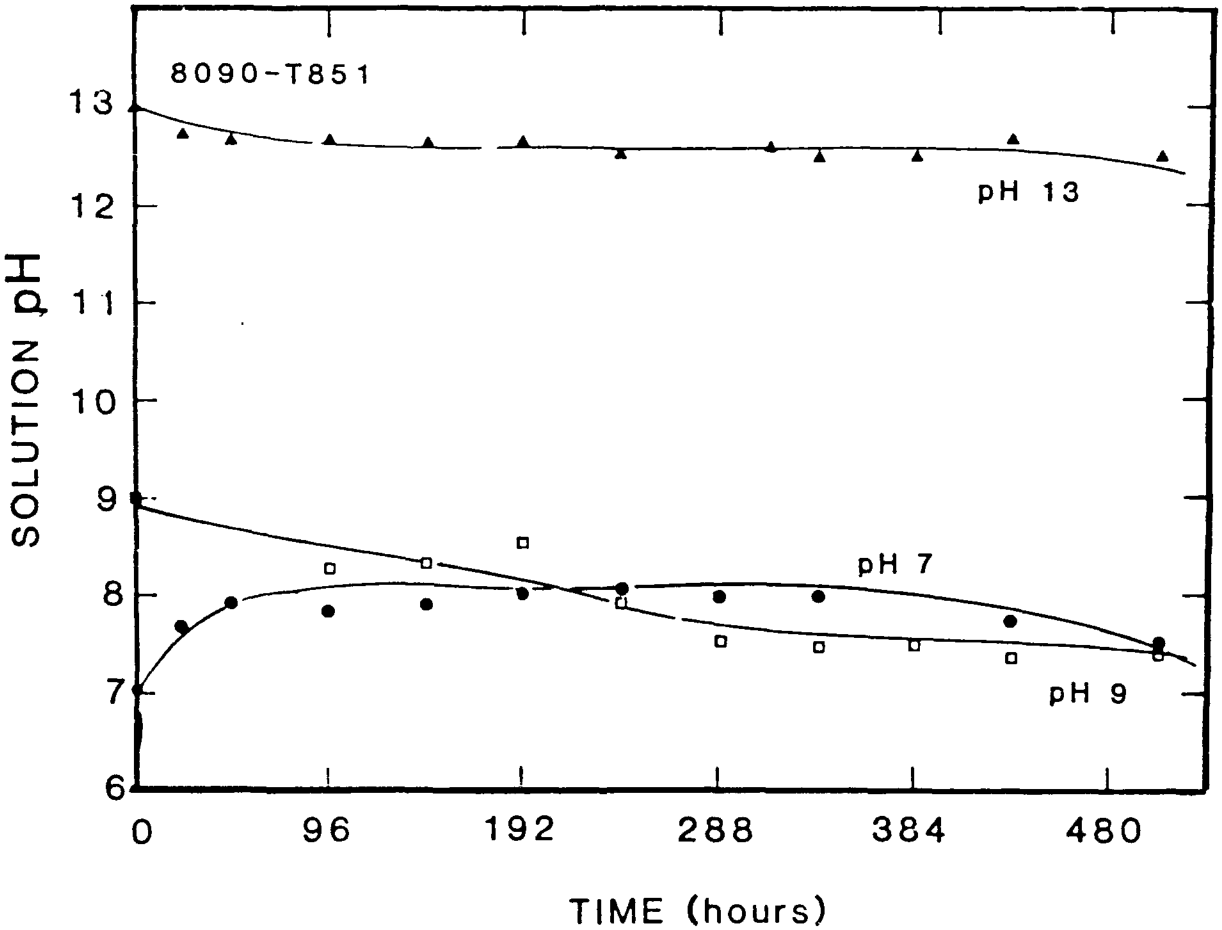

Figure 24. Comparison of the variation of the solution pH of basic solutions and the neutral solution (pH 7).

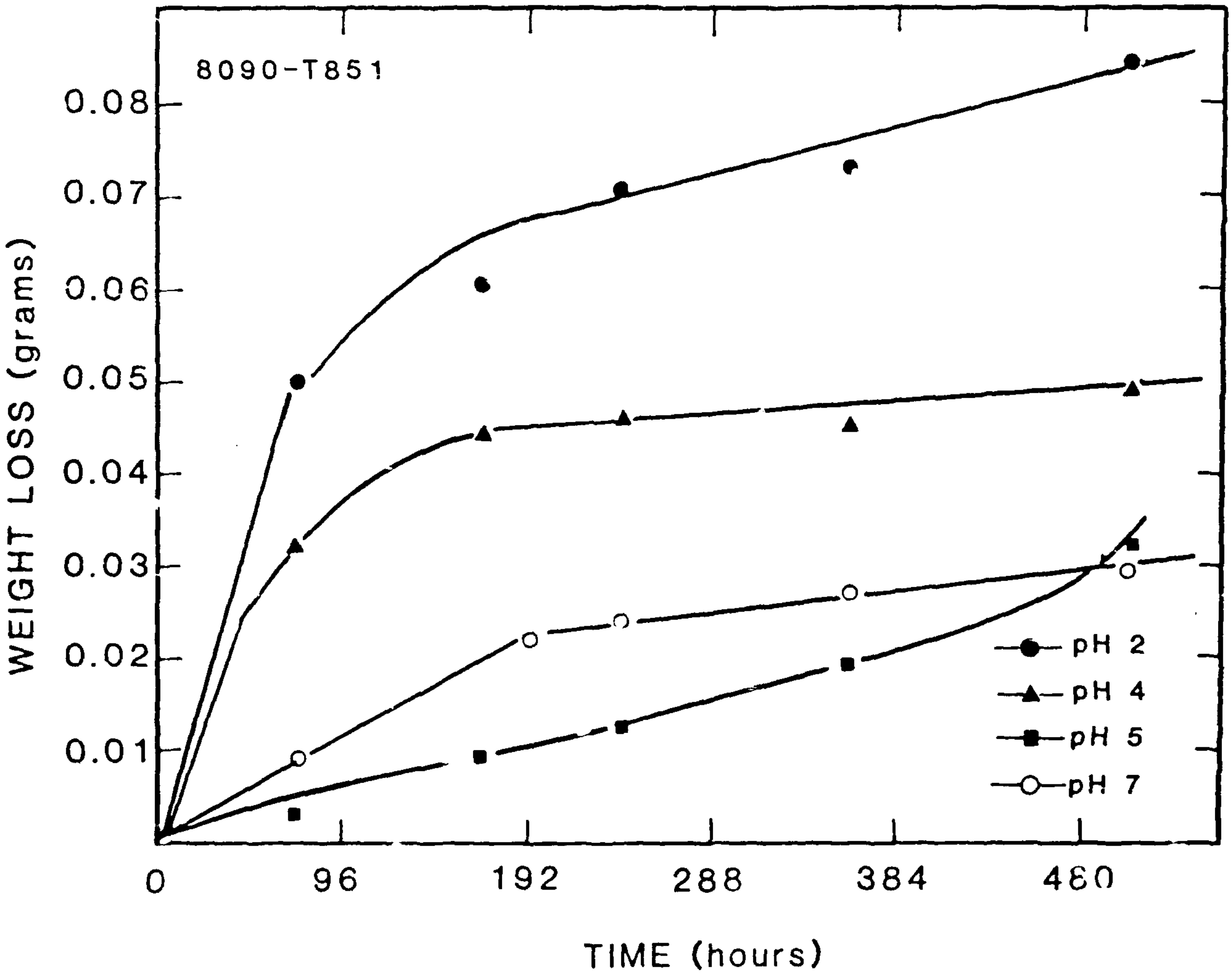

Figure [illegible]. The variation of weight loss (grams) with time (hours) in aqueous solutions of pH 2, pH 4, pH 5 and pH 7.

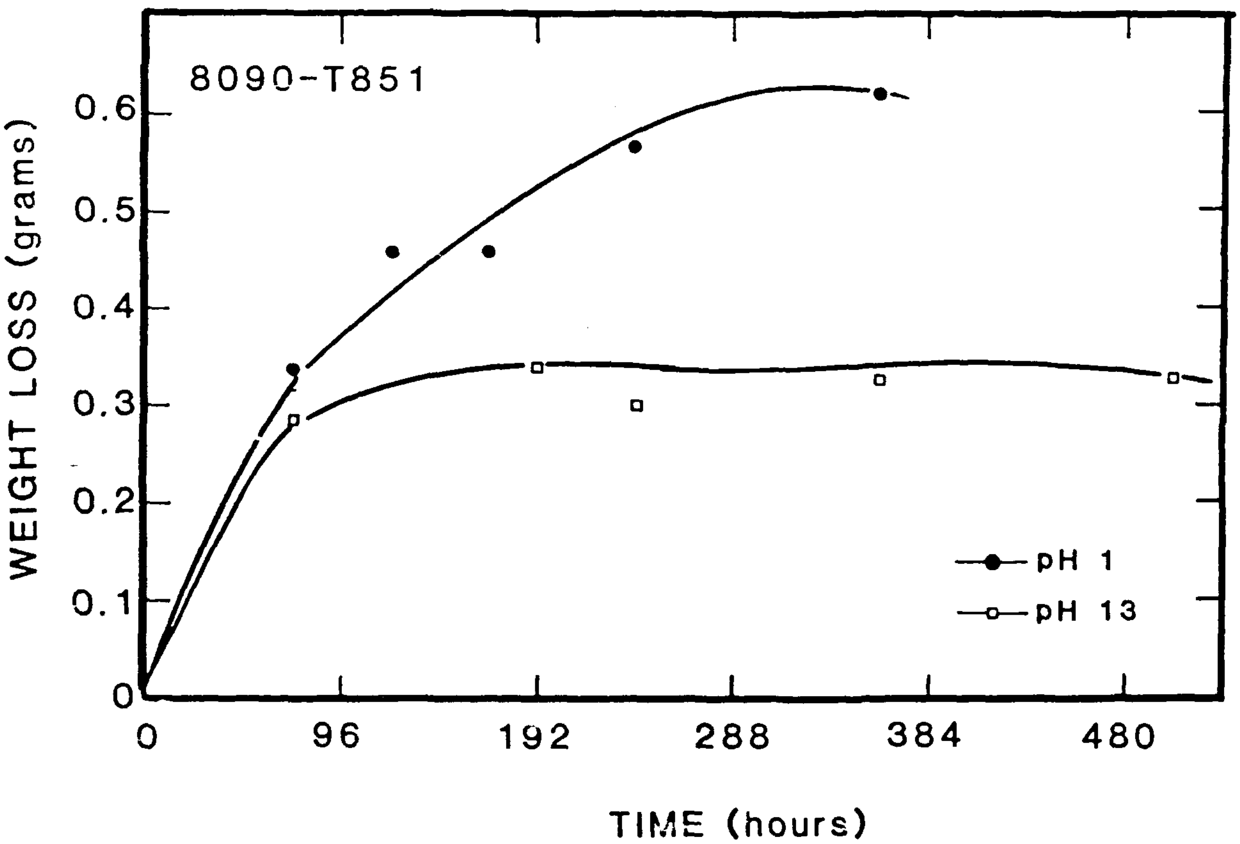

Figure 26. The variation of weight ' (grams) with time (hours) in aqueous soluuc..s of pH 1 and pH 13.

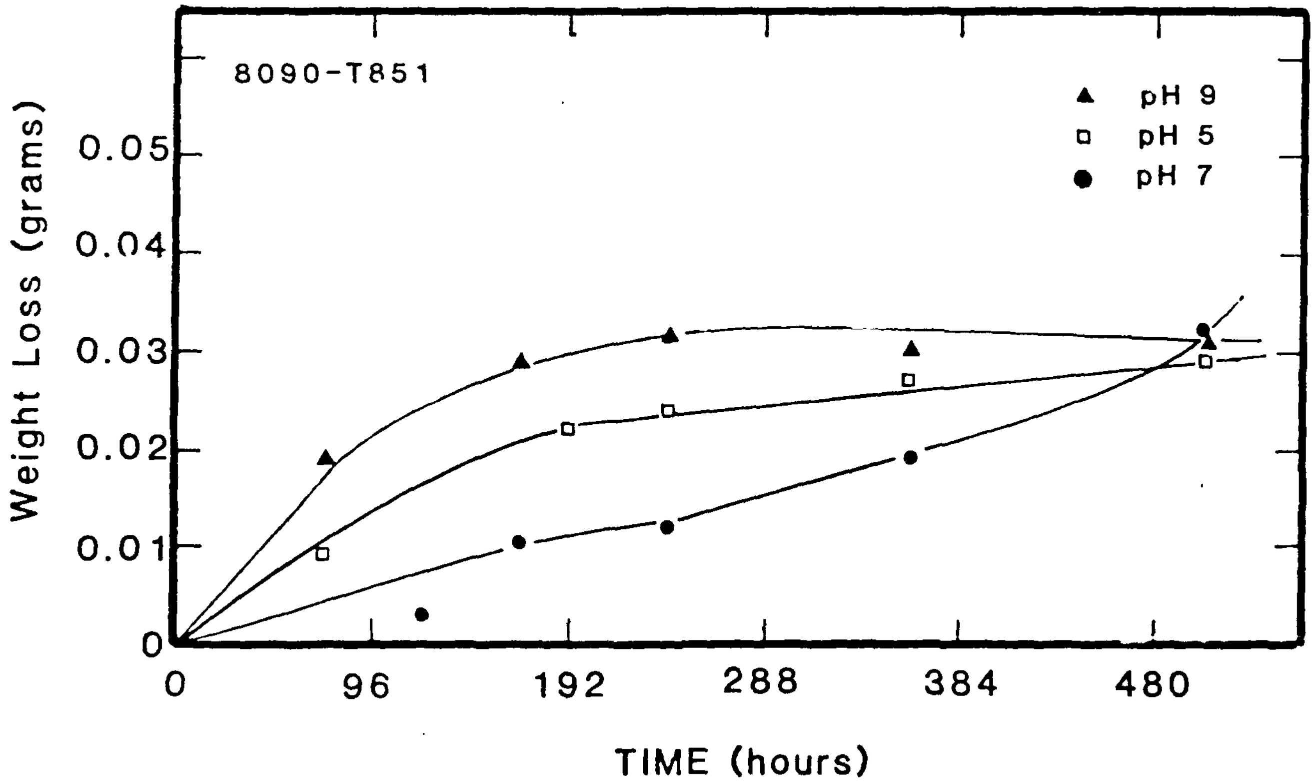

Figure 27. Comparison of the variation of weight loss (grams) with time (hours) in the neutral solution with that in an acidic solution (pH 5) and a basic solution (pH 9).

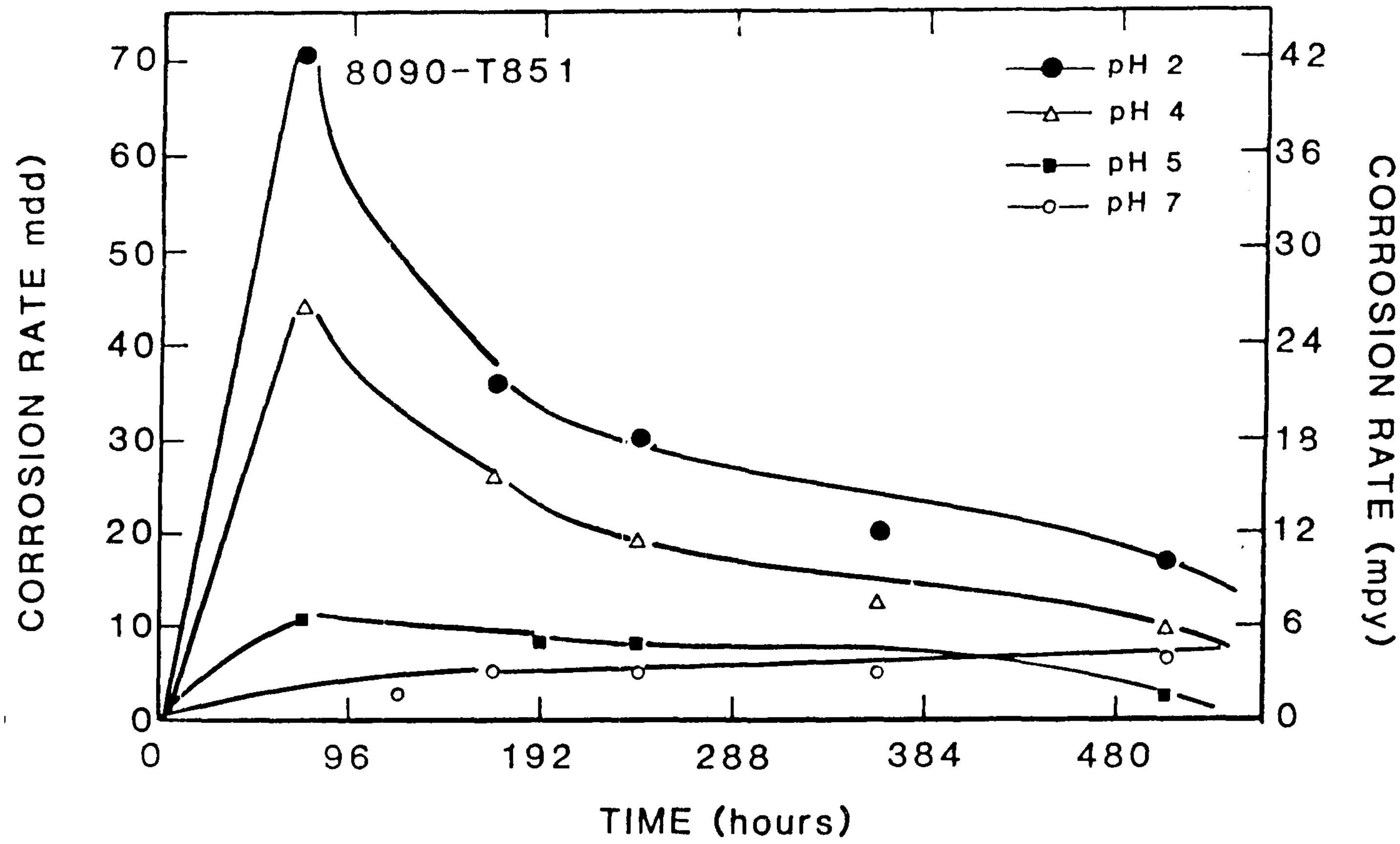

Figure 28. Comparison of the variation of corrosion rates of aluminum alloy 8090-T851 in acidic solutions (pH 2, pH 4 and pH 5) and in the neutral solution (pH 7).

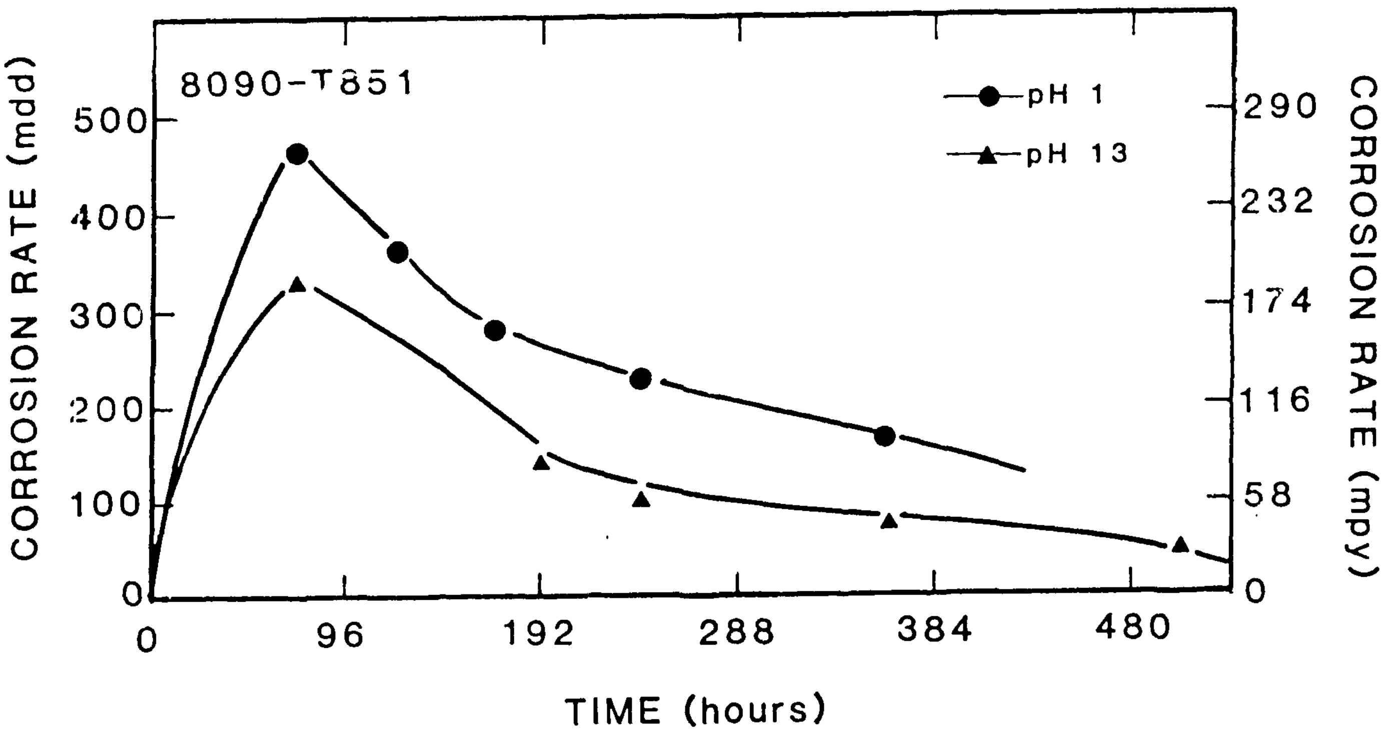

Figure 29. Comparison of the variation of corrosion rates of aluminum alloy 8090-T851 with time (hours) in solutions of pH 1 (acidic) and pH 13 (basic).

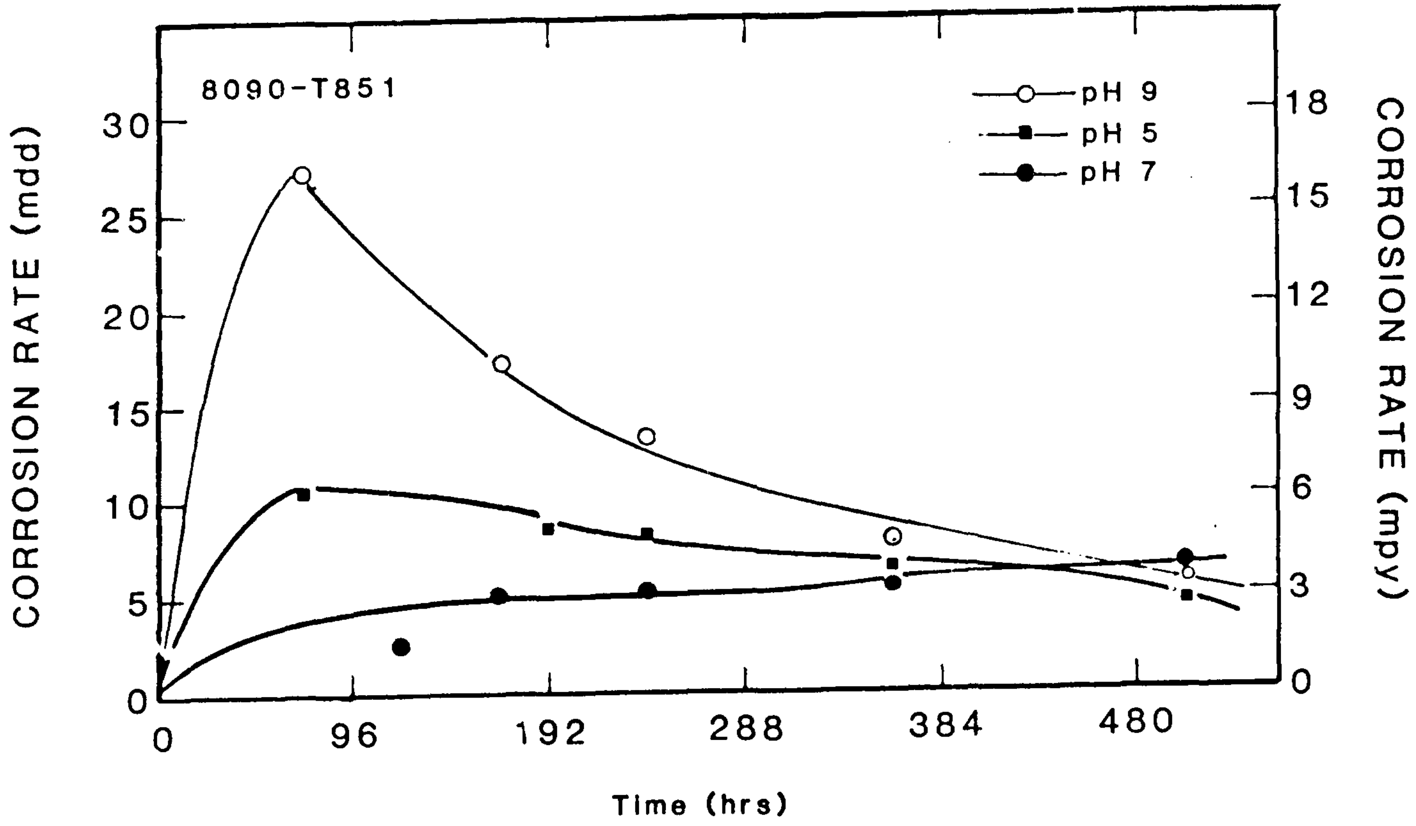

Figure 30. Comparison of variation of corrosion rates with time (hours) of alloy 8090-T851 in an acidic, a basic and the neutral solution.

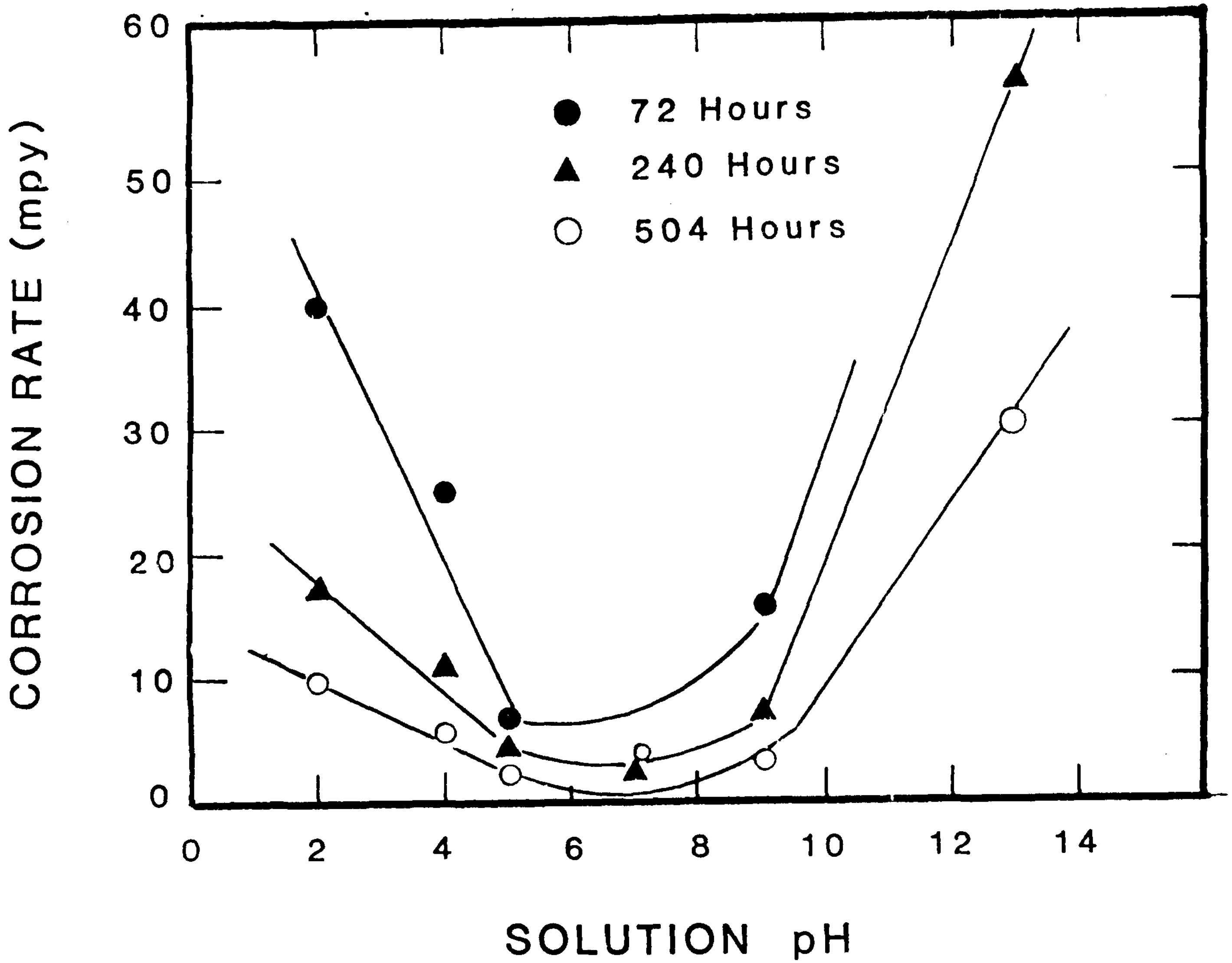

Figure 31. Variation of corrosion rate (mpy) with solution pH.

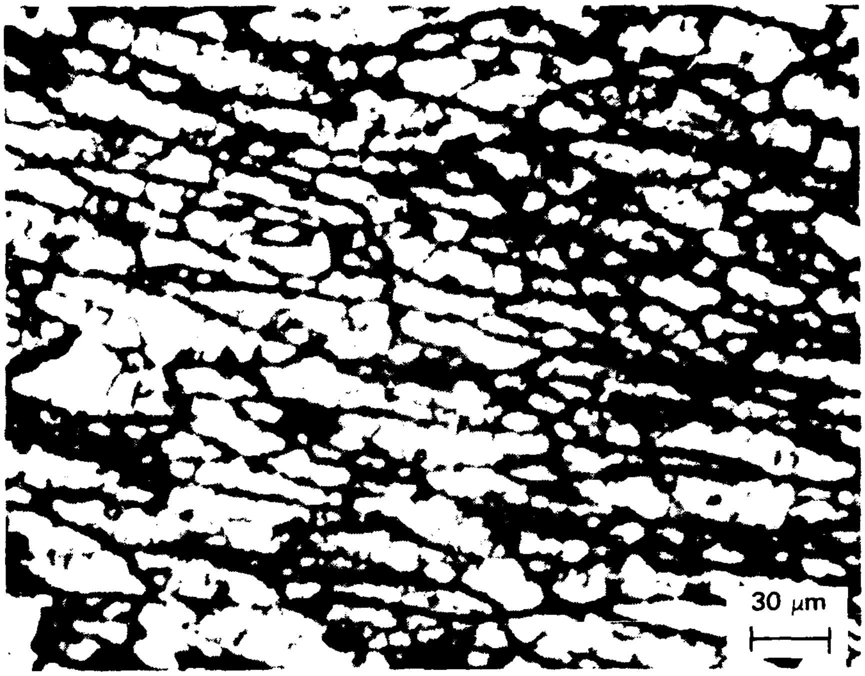

FIGURE 32. OPTICAL MICROGRAPH OF Al-2.8Li-1.3Cu-0.7Mg-0.12Zr SAMPLE SHOWING INTERGRANULAR ATTACK AND PITS AFTER IMMERSION FOR 72 HOURS (3 DAYS) IN SOLUTION OF pH 2

FIGURE 33. SCANNING ELECTRON MICROGRAPH OF THE Al2.8Li-1.3Cu-0.7Mg SAMPLE SHOWING INTERGRANULAR ATTACK ALONG THE GRAIN BOUNDARIES AND PIT FORMATION AFTER IMMERSION IN SOLUTION OF pH 2 for 72 HOURS

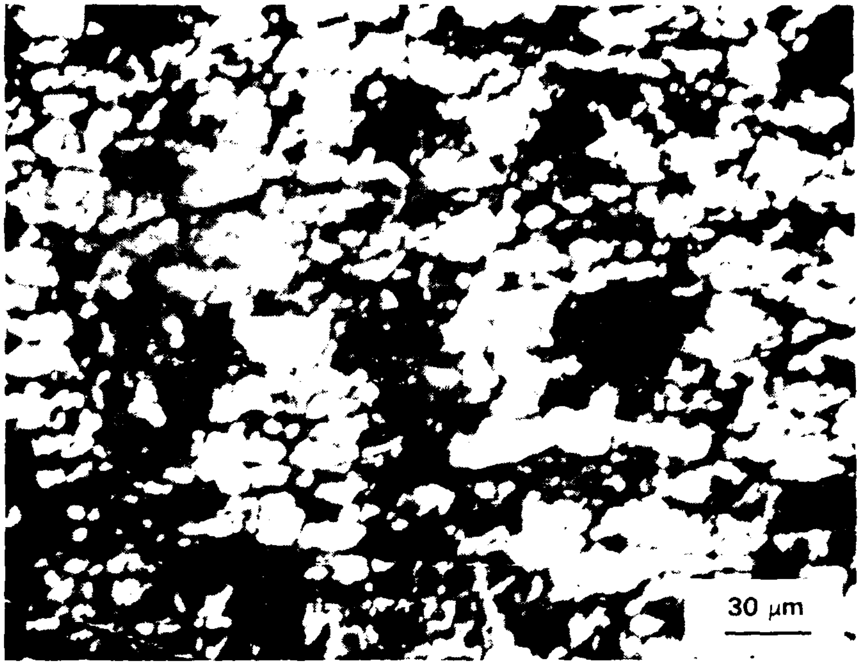

FIGURE 34. OPTICAL MICROGRAPH OF Al-2.8Li-1.3Cu-0.7Mg-0.12Zr SAMPLE SHOWING EXTENSIVE INTERGRANULAR ATTACK AND PITTING AFTER IMMERSION FOR 240 HOURS IN SOLUTION OF pH 2

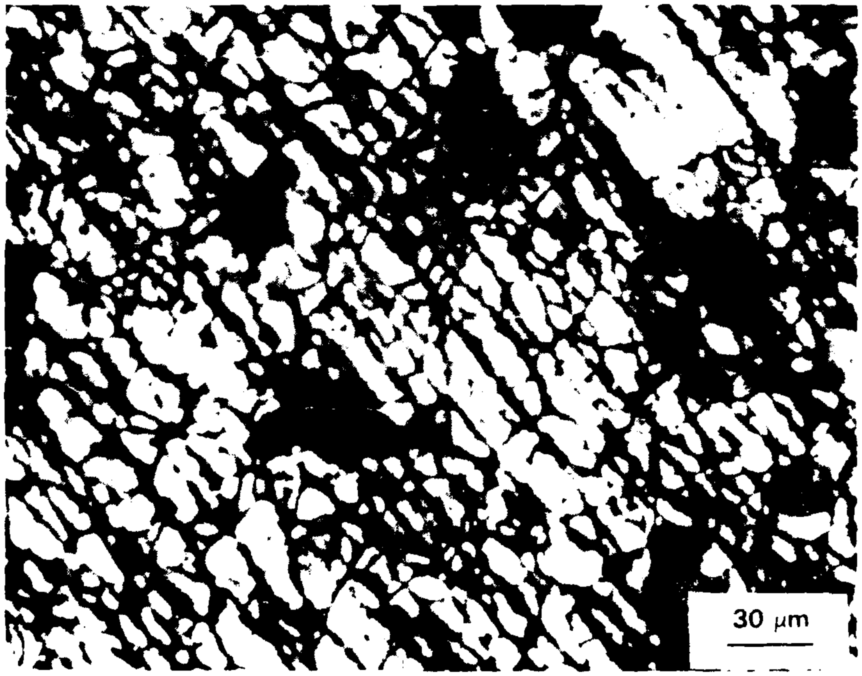

FIGURE 35. OPTICAL MICROGRAPH OF THE Al-2.8Li-1.3Cu-0.7Mg SAMPLE AFTER IMMERSION FOR 504 HOURS IN SOLUTION OF pH 2

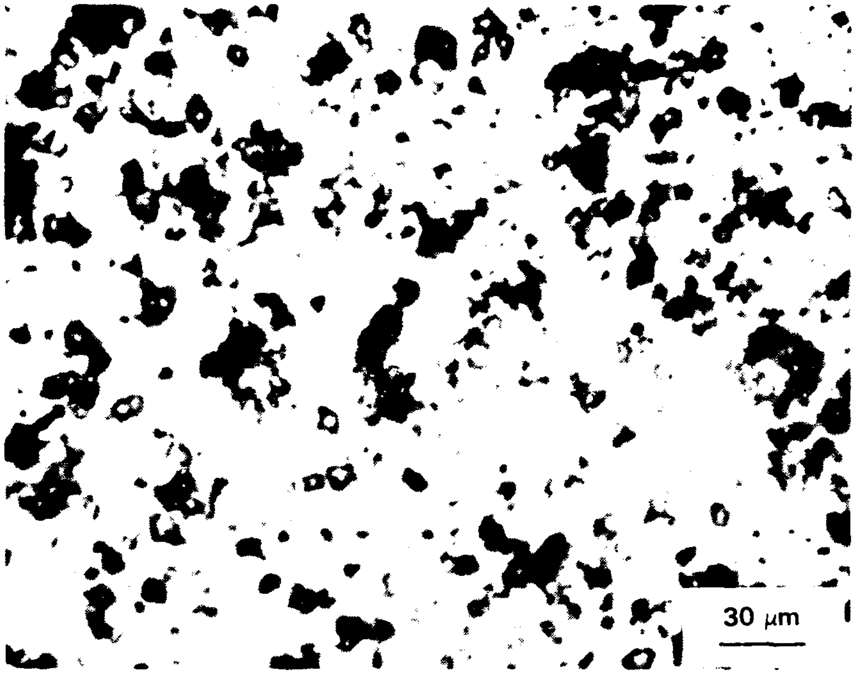

FIGURE 36. OPTICAL MICROGRAPH OF Al-2.8Li-1.3Cu-0.7Mg-0.12Zr SAMPLE SHOWING PIT FORMATION AT SECOND-PHASE PARTICLES DISPERSED IN THE MATRIX AFTER IMMERSION FOR 72 HOURS IN SOLUTION OF pH 4

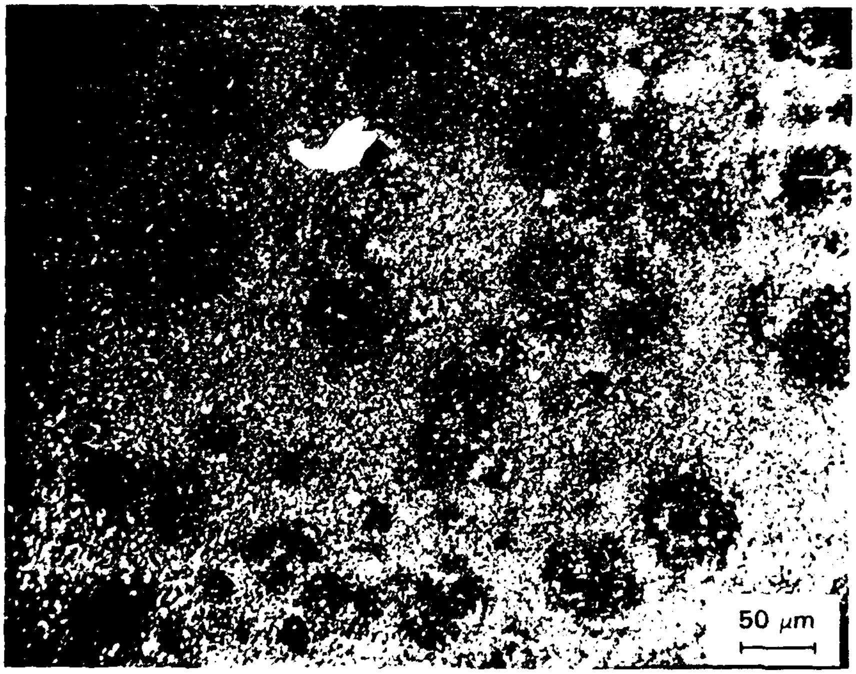

FIGURE 37. SCANNING ELECTRON MICROGRAPH SHOWING PIT SIZE AND NUMBER DENSITY IN Al-2.8Li-1.3Cu-0.7Mg SAMPLES IMMERSED FOR 72 HOURS IN SOLUTION OF pH 4

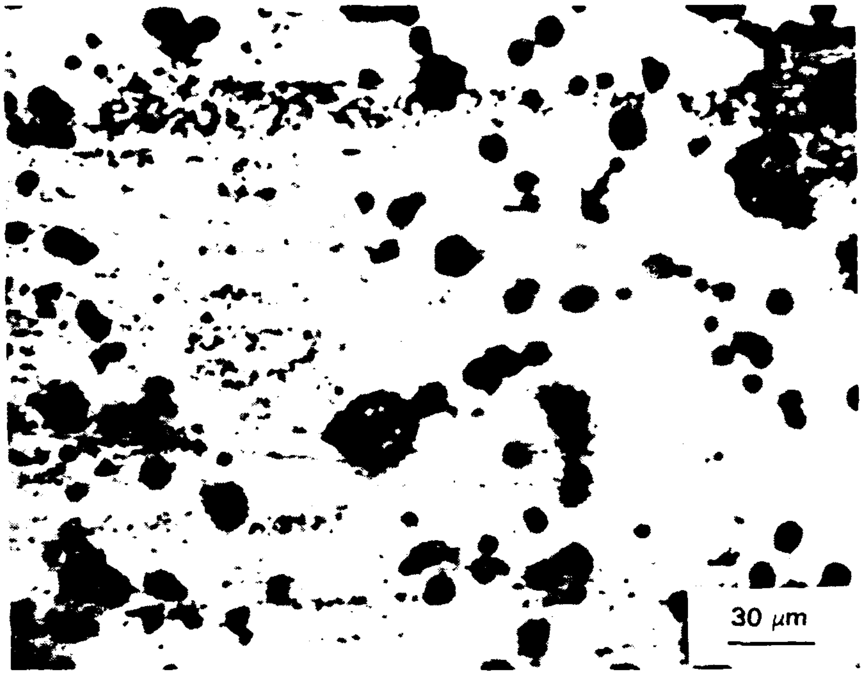

FIGURE 38. OPTICAL MICROGRAPH OF THE Al-2.8Li-1.3Cu-0.7Mg-0.12Zr SAMPLE SHOWING PIT FORMATION AFTER IMMERSION FOR 72 HOURS IN SOLUTION OF pH 5

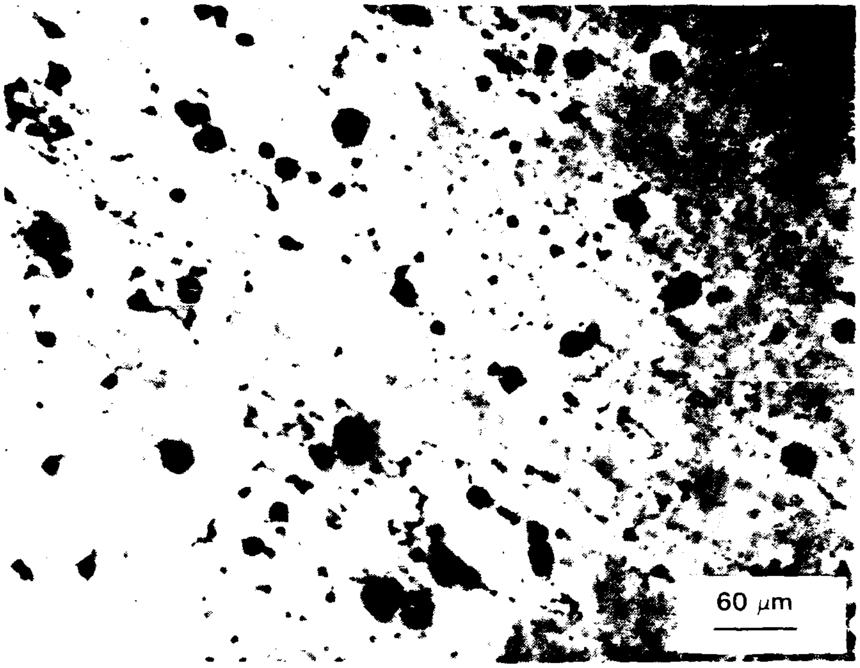

FIGURE 39. OPTICAL MICROGRAPH OF Al-2.8Li-1.3Cu-0.7Mg-0.12r SAMPLE AFTER IMMERSION FOR 72 HOURS IN THE NEUTRAL SOLUTION (pH 7)

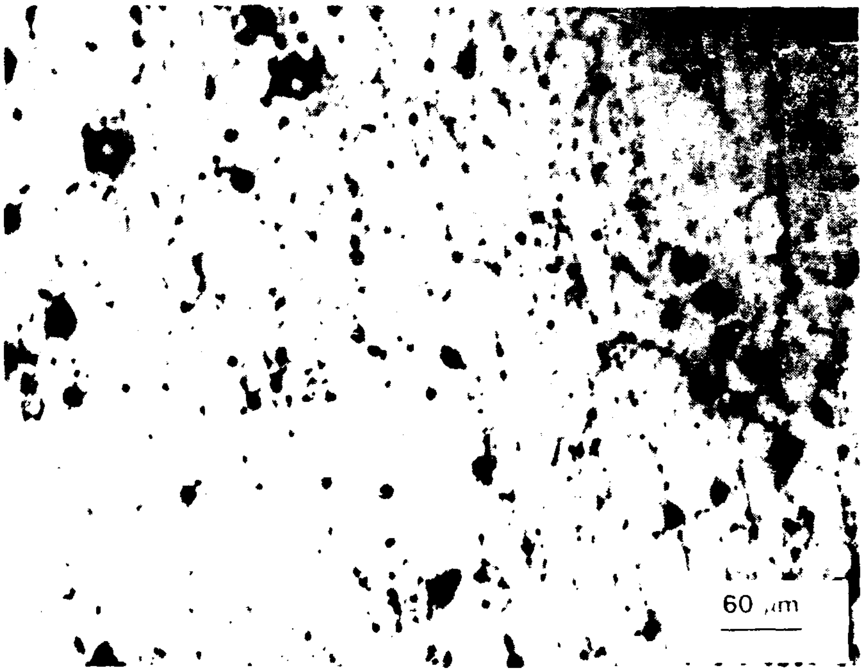

FIGURE 40. OPTICAL MICROGRAPH OF THE Al 2.8Li 1.3Cu 0.7Mg 0.12Zr SAMPLE AFTER IMMERSION FOR 120 HOURS IN THE NEUTRAL SOLUTION (pH 7)

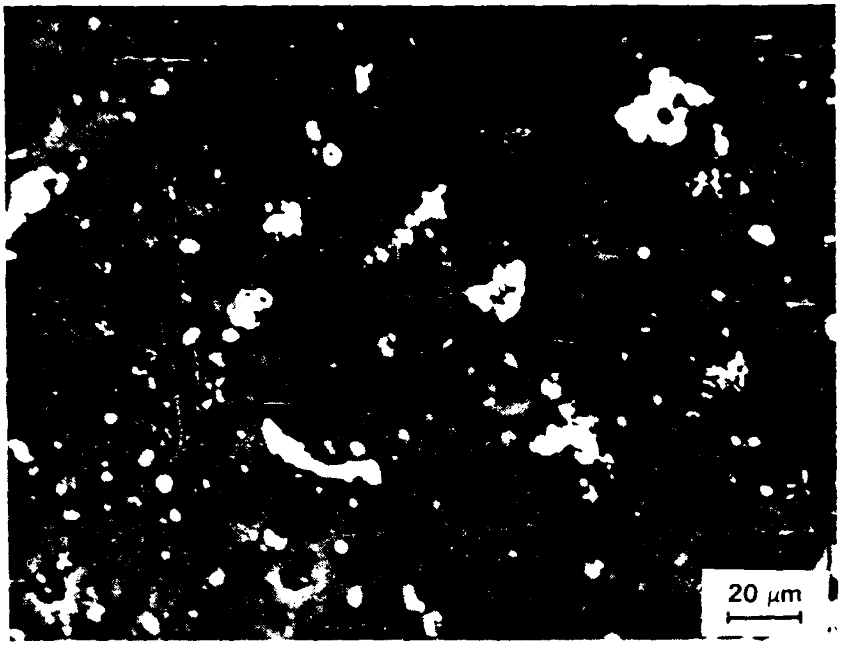

FIGURE 41. SCANNING ELECTRON MICROGRAPH SHOWING THE SIZE AND DISTRIBUTION OF PITS IN THE SAMPLE IMMERSED IN THE NEUTRAL SOLUTION FOR 240 HOURS

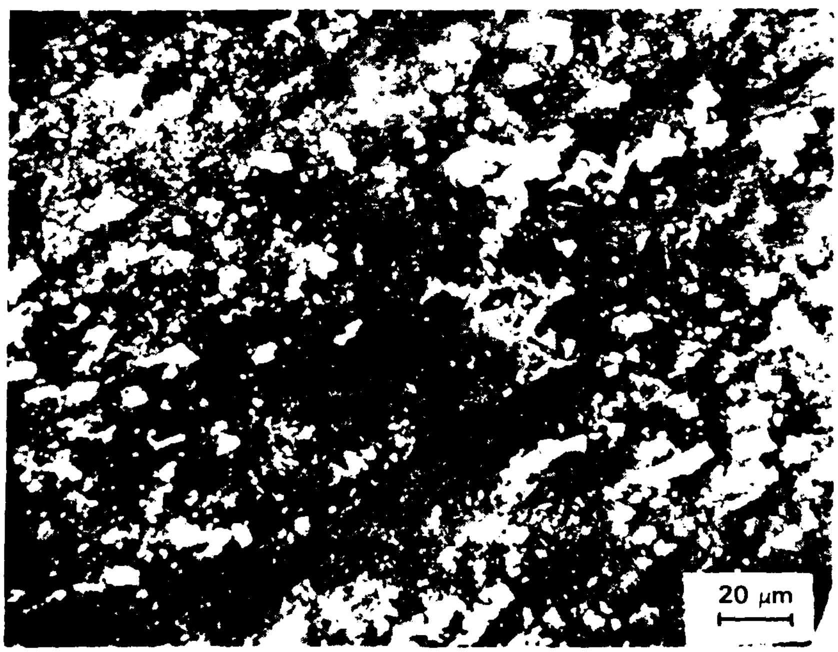

FIGURE 42. SCANNING ELECTRON MICROGRAPH SHOWING DISTRIBUTION AND SIZE OF THE PITS FORMED IN THE SAMPLE IMMERSED IN SOLUTION OF pH 9, FOR 240 HOURS

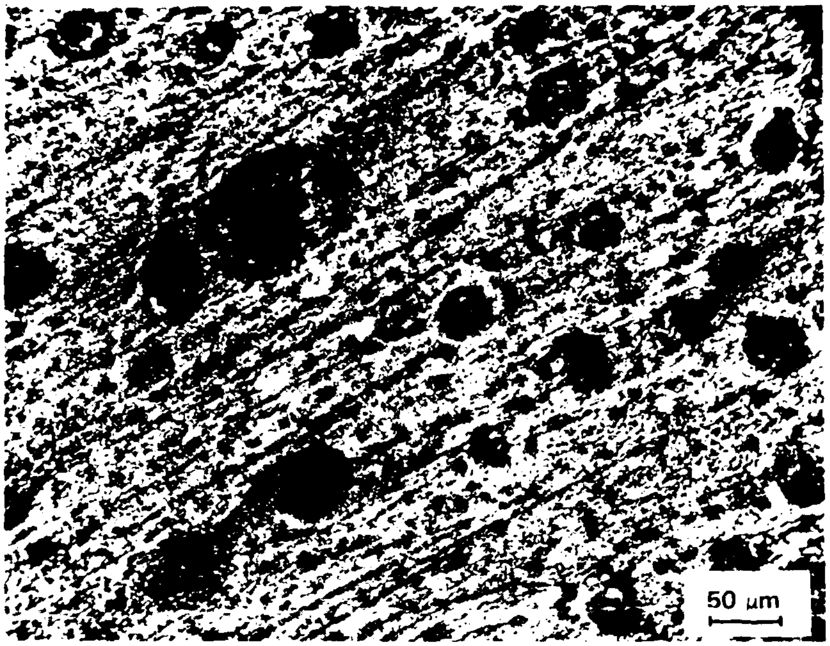

FIGURE 43. SCANNING ELECTRON MICROGRAPH SHOWING FEATURES ON THE SURFACE OF THE Al-2.8Li-1.3Cu-0.7Mg-0.12Zr SAMPLE EXPOSED TO SOLUTION OF pH 9 FOR 72 HOURS

APPENDIX - I

CORROSION COUPONS
Al-Li-Cu-Mg-Zr ALLOY 8090
pH 2

72 HRS | 240 HRS | 504 HRS

FIGURE I-1. COMPARISON OF THE APPEARANCE OF Al-2.8Li-1.3Cu-0.7Mg-0.12Zr ALLOY SPECIMENS (COUPONS) SURFACES AFTER IMMERSION FOR VARIOUS TIME INTERVALS IN SOLUTION OF pH 2, TO HIGHLIGHT THE EXTENT OF DEGRADATION WITH IMMERSION TIME

CORROSION COUPONS
Al-Li-Cu-Mg-Zr ALLOY 8090
pH 7

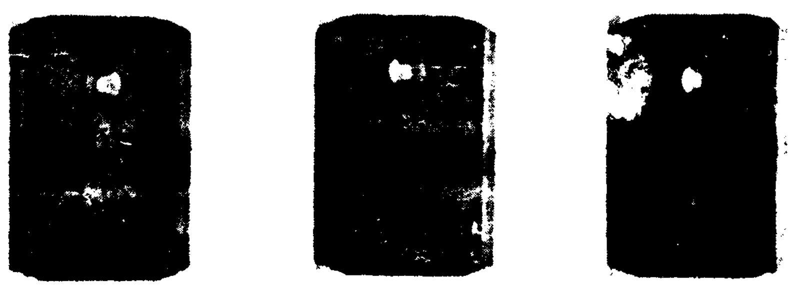

120 HRS | 240 HRS | 504 HRS

FIGURE I-2. COMPARISON OF THE APPEARANCE OF Al-2.8Li-1.3Cu-0.7Mg-0.12Zr ALLOY SPECIMENS (COUPONS) AFTER IMMERSION FOR VARIOUS TIME INTERVALS IN THE NEUTRAL SOLUTION (pH 7), TO HIGHLIGHT THE EXTENT OF SURFACE DEGRADATION WITH IMMERSION TIME

CORROSION COUPONS
Al-Li Cu-Mg-Zr ALLOY 8090
pH 9

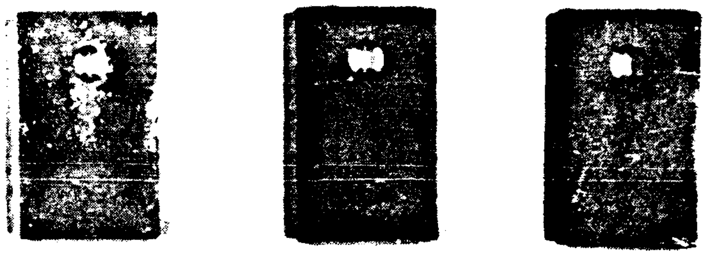

72 HRS 24 HRS 504 HRS

FIGURE I-3. COMPARISON OF THE APPEARNCE OF Al-2.8Li-1.3Cu-0.7Mg-0.12Zr ALLOY SPECIMENS (COUPONS) AFTER IMMERSION FOR VARIOUS TIME INTERVALS IN SOLUTION OF pH 9 (BASIC SOLUTION), TO HIGHLIGHT THE EXTENT OF DEGRADATION WITH IMMERSION TIME. SPECIMEN SURFACES CLEANED IN DISTILLED WATER AND DEGREASED IN ACETONE TO HIGHLIGHT SURFACE FEATURES

CORROSION COUPONS
Al-Li-Cu-Mg-Zr ALLOY 8090
72 HOURS

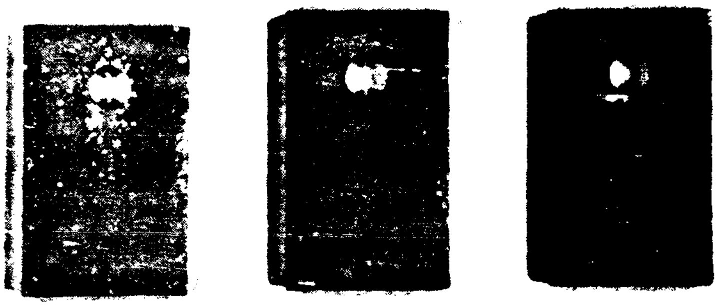

pH 9 pH 11 pH 13

FIGURE I-4. COMPARISON OF THE APPEARANCE OF Al-2.8Li-1.3Cu-0.7Mg-0.12Zr ALLOY SPECIMENS AT CONCLUSION (72 HOURS) OF THE IMMERSION TEST. SPECIMEN SURFACE CLEANED WITH DISTILLED WATER AND DEGREASED WITH ACETONE TO HIGHLIGHT THE SURFACE FEATURES

CORROSION COUPONS
Al-Li-Cu-Mg-Zr ALLOY 8090
240 HRS

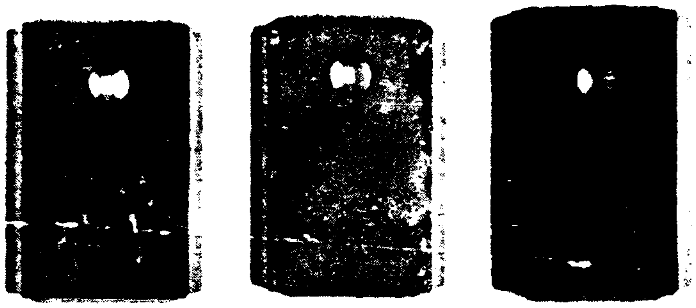

pH 2 pH 7 pH 11

FIGURE I-5. COMPARISON OF THE APPEARANCE OF Al-2.8Li-1.3Cu-0.7Mg-0.12Zr ALLOY SPECIMENS AT CONCLUSION (240 HOURS) OF THE IMMERSION TEST. SPECIMEN SURFACE CLEANED WITH DISTILLED WATER AND ACETONE TO HIGHLIGHT THE SURFACE FEATURES